In compliance with the
Canadian Privacy Legislation
some supporting forms
may have been removed from
this dissertation.

While these forms may be included
in the document page count,
their removal does not represent
any loss of content from the dissertation.

Studies of Coarsening in Hexagonal Patterns

Marianne Roussy

Centre for the Physics of Materials
Department of Physics, McGill University
Montréal, Québec

A thesis submitted to the
Faculty of Graduate Studies and Research
in partial fulfillment of the requirements for the degree of
Master of Science

Your file Votre référence
ISBN: 0-612-88287-X
Our file Notre référence
ISBN: 0-612-88287-X

Acknowledgments

I would like to thank Martin Grant, my supervisor, for his advice and support during the course of my graduate studies, and for having suggested the study of this interesting project in the first place. I am also greatly indebted to Martin Dubé for his immense help throughout the past years. Merci infiniment.

I gratefully acknowledge the financial support of the Natural Sciences and Engineering Research Council of Canada in the form of a graduate scholarship. My thanks also go to my office collegues, and more particularly Andrei, Khosrow and Nela, for an enjoyable atmosphere. And finally, a big hug to Isabelle, Louis-Eric, Randy and Simon, et un merci tout spécial à Bernard Couët. You've all helped me in one way or another.

Résumé

Nous présentons une approche décrivant la formation et l'évolution d'une surface comportant une structure hexagonale, grâce à l'utilisation d'un champ de phase. Nous avons étudié une énergie libre et une équation dépendante en temps de Ginzburg-Landau, pour laquelle le paramètre d'ordre est non-conservé. Nous passons en revue le phénomène des lois d'échelle en général, suivi d'une revue des systèmes hexagonaux en particulier, tant aux points du vue expérimental que théorique. Nous avons utilisé, pour les simulations, une grille carrée comportant des conditions aux frontières périodiques. Nous avons débuté notre étude par l'évolution des surfaces comme telles. Puis, nous avons étudié l'évolution de l'amplitude maximale du facteur de structure, suivie de l'évolution de sa largeur à mi-hauteur. Nous avons également déduit des lois d'échelle pour ces variables. Nous avons aussi étudié les énergies de surface. Nous avons, en effet, regardé l'évolution des énergies de surface en fonction du temps et en avons déduit une loi d'échelle pour les énergies. Finalement, nous avons étudié l'évolution des functions de corrélations temporelles. Nous proposons également une loi d'échelle pour ces dernières.

Abstract

A phase-field approach describing the formation and evolution of an hexagonally patterned surface is presented. We studied a free-energy and a time-dependent Ginzburg-Landau equation for which the order parameter is non-conserved. We give a review of the scaling phenomena in general and of hexagonal systems in particular, both from theoretical and experimental points of views. A squared shaped grid of varied sizes, with periodical boundary conditions, was used for the simulations. First, we studied the evolution of surfaces themselves. Then, we considered the evolution of the structure factor's maximum amplitude, and full width at half maximum. Scaling laws as a function of system size were found for these variables. We also made a study of surface energies. We monitored the evolution of the surface energies with time, and propose a scaling law for the energies. Finally, we studied the evolution of temporal correlation functions. We propose a further scaling law for the temporal correlation functions.

Contents

List of Figures

Chapter 1

Introduction

The number and diversity of systems in an unstable or metastable state, which have been studied either experimentally or theoretically, is enormous. For example, simple fluids, binary fluids[23], gels, lasers, polymer blends, and even astrophysics are all related in one way or another to the time evolution of unstable systems. Many experimental measurements have been conducted concerning the formation and growth of regular domains evolving from an irregular pattern. Studies on electroconvection[37] or diblock copolymers[40], to only name two, are good examples. This work aims at describing the behaviour of a particular system in an unstable or metastable state, the formation of hexagonal patterns on a surface. For a proper understanding of metastability, a dynamical description is required. Therefore, a theory of the time evolution of phase separation in a system is needed.

Understanding metastable and unstable states involves systems which are far from equilibrium. With this in mind, the processes of random interface formation, motion and transformation also represents an interesting topic to study. Furthermore, when considering the evolution of systems with time, one often sees self-similarity. Thus dynamical scaling is often involved in the evolution of phase separating systems. Systems which are different can be related by their scaling behaviour, which determines their universality class. Indeed, if we consider the order parameter, whether the latter is locally conserved or not will lead to different models such as Model A and Model B, belonging to different universality classes, as will be discussed.[8][29][24]

A wide variety of nonequilibrium systems form cellular hexagonal patterns. For example, volcanic basalt columns and nanometer-scale anodization pores. Other examples are common in nonlinear optics, chemistry, and biology.[17] In fact, many articles written on experiments or theoretical simulations presently conducted, either on Rayleigh-Bénard convection in non-Boussinesq fluids[15][16][6], Bénard-Marangoni convection[43][13][5], autocatalytic reactions[35] or block co-polymers[3] mention the appearance of hexagonal or striped patterns. The focus of these works considers the dynamics of dislocations[38], the dynamics of penta-hepta defects[43][44][45], wavelength selection mechanisms, coarsening, the motion of grain boundaries[7] or the formation of the hexagonal paterns themselves[35].

Here we present a model of hexagonal pattern formation, and investigate its properties. Our model simulates phase separation and can be applied to realistic materials. The model is not restricted by common problems of molecular dynamics simulations, such as atomic sizes and phonon time scales, or by continuum field theories for which it is difficult to incorporate the appropriate physics. Our model aims at describing phenomena on mesoscopic length and time scales, including the essential physics, not limited by atomic time scales.

A brief outline of the thesis follows. Chapter 2 explains the qualitative features of first-order phase transitions. Order parameters, the Landau free-energy equations, scaling theory, and stochastic dynamical models such as model A and model B are described. Concluding this chapter is a brief introduction to the equations used in the present simulation, i.e. the specific Landau free-energy and the stochastic model used. Chapter 3 reviews the experimental and theoretical studies relating to systems similar to the one presented here. Chapter 4 gives a description of the simulations performed and the results obtained. It is subdivided into three independent sections, one concerning the structure factor, one concerning surface energy, and the last one concerning temporal correlations. A conclusion follows, summarizing the major results of the thesis and outlining future directions for research on similar systems.

Chapter 2

Phase Transitions, Scaling and Dynamical Models

2.1 General Features

To illustrate the concept of a phase transition, consider a magnet.[22] At high temperature T, and when no external field is present, the system is in the paramagnetic phase. This means that spins point randomly in all directions. Thus, there is no net magnetic moment, $M = 0$. However, below a critical temperature T_c, and even without an external field applied, the spins tend to align along a particular direction. In this case, there is a non-zero net magnetization $M(T)$, and the system is in the ferromagnetic state. All directions are equivalent, but only one will be selected. This corresponds to the symmetry breaking process. The onset of this behaviour is a continuous phase transition, i.e. the magnetization rises continuously from zero as the temperature is reduced below T_c. There is no discontinuity and this phase transition is therefore a continuous or second-order transition: there is no generation of latent heat.

Systems quenched from a disordered phase, into a thermodynamically metastable or unstable state, ultimately reach an ordered phase, after evolving over a certain period of time. In fact, we usually witness a competition taking place between the different broken-symmetry phases to select the equilibrium state. A network of domains of the different competing equilibrium phases develops, for which the length scale increases

with time. Also it is important to note that, in the thermodynamic limit, final equilibrium is never achieved. In fact, in the ordered phase, the longest relaxation time diverges with the system size. Also, it is generally the initial fluctuations in the system which induce the appearance and the development of the network of domains. These fluctuations are amplified during competitive growth. The amount of time taken by a system to approach final equilibrium will thus be affected by these fluctuations present in the system, as well as by the existence of many different nearly stationary configurations, in which the system can settle.[1]

The order parameter of a system, ϕ, determines the amount of local order in this system. For example, a convenient order parameter for the Ising model is magnetization. The models we shall study are closely related to the "Ising universality class", meaning the order parameters considered are simple one-component quantities, as opposed to vectors, tensors, complex numbers, or the like. Therefore, it is convenient to set up a continuum description in terms of a coarse-grained order parameter scalar field $\phi(\vec{x}, t)$ as a function of position $\vec{x}$ and time t. Such a description is straightforward to solve numerically. A suitable Landau free-energy functional to describe the ordered phase is

$$F[\phi] = \int d^d x[\kappa/2|\vec{\nabla}\phi|^2 + V(\phi)], \tag{2.1}$$

where the potential $V(\phi)$ has a double-well structure[29][8], (see fig. (2.1))

$$V(\phi) = (1/A)(1-\phi^2)^2, \tag{2.2}$$

and κ and A are constants.
The terms have the following origins: the potential $V(\phi)$ ensures there are two coexisting thermodynamic phases, and the gradient-squared term associates an energy cost with inhomogeneity in space.[26] Indeed, since grain boundaries are in general non-equilibrium features, they have a positive excess free energy. In some systems, the gradient is negative, in which case we need to consider higher order terms in the expansion because we still need an energy cost associated with the presence of an interface. We thus arrive at a free-energy functional of this type:

$$F[\phi] = \int d^d x[1/2|\vec{\nabla}^2\phi|^2 - {q_0}^2|\vec{\nabla}\phi|^2 + V(\phi)], \tag{2.3}$$

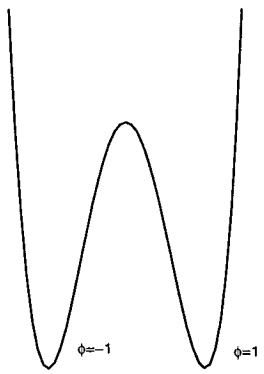

Figure 2.1: Example of double-well structure

where q_0 sets the scale for internal structure such as stripes or circles, and the potential $V(\phi)$ still has a double-well structure.

Initially, different domains are formed, separated by well defined interfaces. At later times, phase ordering takes place through the motion of these interfaces. General theories of domain coarsening have been developed based on the idea that, although the domain structure is evolving, it remains statistically self-similar at all-times (see figure (2.2)). This leads to the concept of dynamic scaling which assumes the existence of a unique characteristic length $L(t)$ for which, when lengths are scaled by $L(t)$ and we are at late times, the domain structure is independent of time. In the dynamic scaling regime, L is found to grow as a power law in time, with an exponent n which depends on dimensionality and the character of the order parameter. This scaling hypothesis has been found to apply to a diversity of systems, and to be unaffected by many of the microscopic details of specific materials. That is, the scaling function and the growth exponent are two features which are common to a large number of systems belonging to the same "universality class". To characterize the dynamical statistical properties of the system, we generally use the equal-time pair correlation function

$$C(\vec{r},t) =< \phi(\vec{x}+\vec{r},t)\phi(\vec{x},t) >,$$

and its Fourier transform, the equal-time structure factor

$$S(\vec{k},t) =< \phi_{\vec{k}}(t)\phi_{-\vec{k}}(t) >,$$

to probe the domain structure. The angular brackets used here indicate an average over initial conditions. If we assume a single characteristic length scale $L(t)$ following the scaling theory, we end up with these scaling forms for the correlation function and the structure factor:

$$C(\vec{r},t) = f(r/L)$$

and

$$S(\vec{k},t) = L^d g(kL),$$

where d is the spatial dimensionality, and $g(y)$ is the Fourier transform of $f(x)$. The scaling limit is defined by $r \gg \xi$ and $L \gg \xi$, with r/L arbitrary, where ξ represents the equilibrium correlation length.[8] For more general scaling laws, it can also be interesting to consider the two-time correlation function

$$C(\vec{r},t_1,t_2) =< \phi(\vec{r},t_1)\phi(\vec{r},t_2) > .$$

Experimentally, the growing domain structure is often studied by means of the transmission electron microscopy (TEM), or neutron or x-ray SAS experiments. In the latter case, it is the scattering intensity which is more particularly studied, since, for example, its width is proportional to the inverse of the domain size. When the average scattering intensity is scaled in units of this time-dependent length, one obtains the scattering function for late times in the form of a time-independent scaling function.[9] The scattering of a conventional incoherent x-ray beam from a random arrangement of domains can only measure the average structure factor $< I > (q,t)$. In order to measure the exact structure factor $I(\vec{q},t)$, a coherent incident beam must be employed. With the very high brillance now available from third generation synchrotron sources, we now have access to sufficiently intense coherent x-ray beams to perform such experiments.[31]

2.2 Characteristics of Stochastic Dynamical Models

The dynamics of a system with a very large number of degrees of freedom cannot easily be described by deterministic equations of motion. However, we can proceed as follows. We identify a small number of variables called macrovariables A_i which describe correctly the macroscopic properties of the system. We then write down a set of phenomenological equations of motion for the A_i's, the other degrees of freedom being simulated by adding random noise terms to the equations of motion. We therefore have $\partial_t A_i(t) = G_i[A_j, t] + \xi_i(t)$, where the G_i's are generally non linear functions of all the macrovariables of the form $\partial F/\partial A_i$, with F the energy of the configuration. The functions $\xi_i(t)$ are random noise terms which are characterized by probability distribution function. Furthermore, we can add that if the noise terms have the following properties:

$$< \xi_i(t) = 0 >,$$

and

$$< \xi_i(t)\xi_j(t') >= 2D_i\delta_{ij}\delta(t - t'),$$

(where the D_i are independent of the macrovariables A_j), the probability distribution $P(A_i, t)$ satisfies the following Fokker-Planck equation[23]:

$$\partial_t P[A_i, t] = -\sum_j \frac{\delta}{\delta A_j}[G[A_i]P] + \sum_j D_j \frac{\delta^2}{\delta A_j^2} P.$$

The equilibrium solution of this is evidently a Maxwell-Boltzmann distribution, $P \sim exp(-F[A]/D)$, which therefore determines $G_i = -\partial F/\partial A_i$. These phenomenological equations can be divided into

different models, such as Model A for a non-conserved order parameter and Model B, for a conserved order parameter. It must be stressed from the outset that both Model A and Model B are too simple to produce quantitatively accurate descriptions of most realistic experimental solutions on all length and time scales. Even considering the simplest Ising-like transitions, the details of the atomic and molecular structures, the specific ways in which these atoms or molecules interact with each other, the way they couple to other degrees of freedom, all will have extensive and

complicated effects. For instance, in solids, lattice vibrations and spin waves are transport mechanisms which may crucially affect the the way the system will react but they are not contained in any of our over simplified pictures. Instead, these models describe mesoscopic to long length and time scales.

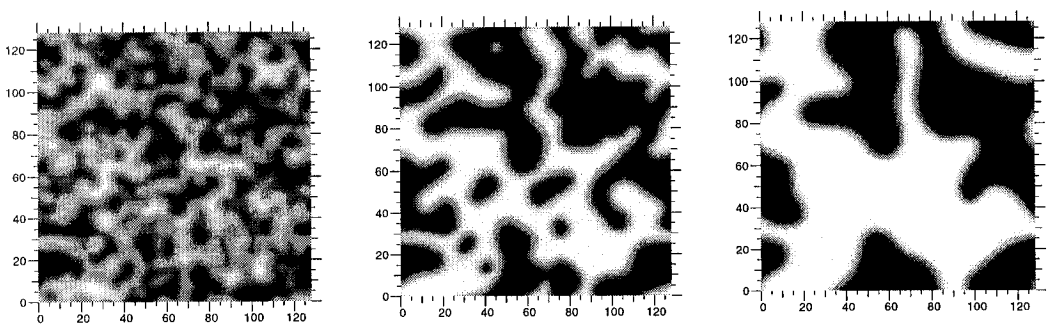

Figure 2.2: Example of symmetry-breaking and phase transition for Model A. These surfaces represent instants after 90 iterations, 350 iterations and 1400 iterations respectively.

2.3 Model A

Model A is the simplest of the stochastic dynamical models. It is concerned with the description of a non-conserved order parameter ϕ, in contact with a constant temperature heat bath. Systems included in this class are the Ising model with spin-flip dynamics, binary alloys undergoing an order-disorder transition, and some magnetic materials with uniaxial anisotropy. To introduce this model, it is most appropriate and easiest to use the Ising model.[22][14] Very briefly, the discretized Ising model is a model of a ferromagnet or antiferromagnet on a lattice of d dimensions. The degrees of freedom, residing on the lattice points are the classical spin variables S_i which can only take two values: up or down ($S_i = \pm 1$). Also, the spins interact with an external magnetic field H, varying from site-to-site.

We can state that such a system is non-conserved since the energy of the spins is transferred quickly to the lattice, and the magnetization appears spontaneously. Therefore, the only slow variable is $\phi(\vec{x}, t)$. As stated earlier, the order parameter of the Ising model is magnetization. When the order parameter is non-conserved, an appropriate equation, using equation (2.1), for the time evolution of the field ϕ is

$$\frac{\partial \phi}{\partial t} = -M \frac{\delta F}{\delta \phi} = M(\nabla^2 \phi - V'(\phi) + H), \tag{2.4}$$

where M is the mobility and $V'(\phi) = \frac{dV}{d\phi}$ (V is defined at equation (2.2)). This equation, generally called the time-dependent Ginzburg-Landau equation, only states that the rate of change in ϕ is proportional to the distance, in function space, of the free energy from equilibrium. When we want to speak of the model A per se, we add a Langevin noise term on the right-hand side. Evidently, as mentioned earlier, the noise term must follow the fluctuation-dissipation theorem:

$$< \zeta(\vec{x}, t) >= 0,$$

and

$$< \zeta(\vec{x}, t)\zeta(\vec{x'}, t') >= 2k_B T M \delta(\vec{x} - \vec{x'})\delta(t - t').$$

where k_B is Boltzmann's constant.

Model A is a purely relaxational model. The magnetization evolves towards the equilibrium value obtained by extremalizing the free energy F. The associated Fokker-Planck equation is simply[23]:

$$\partial_t P[\phi(\vec{x},t)] = M \int d^d\vec{x} \frac{\delta}{\delta\phi(\vec{x},t)}[\frac{\delta P}{\delta\phi(\vec{x},t)} + P\frac{\delta F}{\delta\phi(\vec{x},t)}].$$

Let us now take a closer look at the scaling theory relevant to Model A.[8] If we start from equation (2.4) but consider a single spherical domain of $\phi = -1$ immersed in a sea of $\phi = +1$, and express ∇^2 in spherical coordinates, we end up with (setting $M = 1$ for convenience, and considering $H = 0$)

$$\frac{\partial\phi}{\partial t} = \frac{\partial^2\phi}{\partial r^2} + \frac{d-1}{r}\frac{\partial\phi}{\partial r} - V'(\phi). \tag{2.5}$$

If the droplet radius R is much larger than the interface ξ, we expect $\phi(r,t) = f[r - R(t)]$. Reinserting this equation in the previous, we find

$$0 = f'' + \left(\frac{d-1}{r} + \frac{dR}{dt}\right) f' - V'(f). \tag{2.6}$$

The function $f(x)$ changes from -1 to 1 in a small region of width ξ near $x = 0$. Its derivative will be sharply peaked near $x = 0$. If we multiply equation (2.6) by f' and integrate through the interface, considering $f' = 0$ far from the interface and $V(f)$ has the same value on both sides of the interface, we get

$$0 = \frac{d-1}{R} + \frac{dR}{dt}. \tag{2.7}$$

This equation can also be considered from the point of view of velocity and curvature. Indeed, for a spherical domain, the curvature K is equivalent to $(d-1)/R$, so that $\nu = -\nabla\cdot\hat{g} = -K$ corresponds to equation (2.7), where $\hat{g}$ is a unit vector normal to the wall (in the direction of increasing ϕ). Integrating this latter equation gives $R^2(t) = R^2(0) - 2(d-1)t$, that is the collapse time scales with the initial radius at $t \sim R^2(0)$ or $R \sim t^{1/2}$. Model A is indeed known to scale as

$$L(t) \sim t^{1/2}. \tag{2.8}$$

This scaling law has been verified experimentally. Recent experiments probing scaling further are underway.[20]

2.4 Model B

An extra complication is present in a system where the order parameter ϕ is conserved. Flipping a spin up to a down spin does not cause any problem in the Ising model but it is not the same story if this flipping has to be accompanied by the inverse flipping of the neighbor atom's spin.[28] To take an easier example, consider a binary alloy composed of atoms A and B. For order to take place, atoms A and B have to simultaneously exchange position. Evidently, the total number of atoms A, and atoms B, have to be conserved independently. If there are n_A atoms A and n_B atoms B, then $n_B - n_A$ is equivalent to the magnetization in the Ising model. We can thus choose the concentration of B atoms as an appropriate order parameter. Also, because $E - \mu_A n_A - \mu_B n_B = E - \frac{1}{2}M(\mu_B - \mu_A) - \frac{1}{2}N(\mu_A + \mu_B)$, where $M = n_B - n_A$ and $N = n_B + n_A$. The difference in chemical potentials $\frac{1}{2}(\mu_B - \mu_A)$ plays the same role as the field H in the Ising model. This is also true for Model A.[29]

We should also bear in mind that atoms A and B can generally only exchange positions locally. This will lead to slower growth than for a non-conserved order parameter. In fact, we insist on diffusive transport of the order parameter, and on an equation of motion of the form:

$$\frac{\partial \phi}{\partial t} = M\nabla^2 \frac{\delta F}{\delta \phi} = -2M\nabla^2[\nabla^2\phi - V'(\phi)], \tag{2.9}$$

where M stands for the mobility. One can easily verify that $\int d\vec{x}\phi(x)$ is constant because it is of the form

$$\frac{\partial \phi}{\partial t} = -\vec{\nabla} \cdot \vec{j}, \tag{2.10}$$

where $\vec{j}$ is a current. This equation is generally called the Cahn-Hilliard equation.[12] Again, if we want to consider Model B per se, we have to add a Langevin noise term on the right-hand side of the equation. And here also, the noise term must obey:

$$< \zeta(\vec{x}, t) >= 0,$$

and

$$< \zeta(\vec{x}, t)\zeta(\vec{x'}, t') >= -2k_B T M \nabla^2 \delta(\vec{x} - \vec{x'})\delta(t' - t).$$

The associated Fokker-Planck equation is:

$$\partial_t P[\phi(\vec{x},t)] = -M \int d^d\vec{x} \frac{\delta\nabla^2}{\delta\phi(\vec{x},t)}[\frac{\delta P}{\delta\phi(\vec{x},t)} + P\frac{\delta F}{\delta\phi(\vec{x},t)}].$$

The initial order parameter relaxation time depends on the wave vector k: $\tau(k) \sim k^{-2}$ from ∇^2.[23]

If we now wish to present the scaling theory relevant to Model B, we can start by rewriting equation (2.9) in terms of the chemical potential μ,[8]

$$\frac{\partial\phi}{\partial t} = -\nabla \cdot j,$$

$$j = -\nabla\mu, \tag{2.11}$$

and

$$\mu = \frac{\delta F}{\delta\phi}. \tag{2.12}$$

We wish to consider surfaces of constant ϕ near the interface and introduce a Cartesian coordinate system at each point, with a coordinate g normal to the surface (and increasing with increasing ϕ). Near the interface, the latter equation then becomes

$$\mu = V'(\phi) - \left(\frac{\partial\phi}{\partial g}\right)_t K - \left(\frac{\partial^2\phi}{\partial g^2}\right)_t \tag{2.13}$$

where $K = \nabla \cdot \hat{g}$ is the curvature like in the previous section. The value of μ at the interface can be obtained by multiplying through by $(\partial\phi/\partial g)_t$, which is sharply peaked at the interface, and integrating over g through the interface. We obtain

$$\mu\Delta\phi = \Delta V - \sigma K \tag{2.14}$$

at the interface, where $\Delta\phi$ is the change in ϕ across the interface, ΔV is the difference in the minima of the potential for the two bulk phases, and σ is the surface tension. Now we wish to simplify this equation considering only the case where the minima have equal depth and taking the minima to be at $\phi = \pm 1$ as usual gives $\Delta V = 0$ and $\Delta\phi = 2$,

$$\mu = -\frac{\sigma K}{2}. \tag{2.15}$$

Now, to determine the motion of the interfaces, we use the known fact that $j = -\nabla\mu$ and that a velocity is given by the imbalance between the current flowing into and out of an interface,

$$\nu\Delta\phi = j_{out} - j_{in} = -\left[\frac{\partial\mu}{\partial g}\right] = -[\hat{g}\cdot\nabla\mu], \tag{2.16}$$

where ν is the speed of the interface in the direction of increasing ϕ. Equation (2.12) tells us that $\mu \to 0$ at infinity. If $\partial\phi/\partial t \approx 0$, that is that the system is locally near equilibrium, clearly equations (2.10) and (2.11) imply that μ obeys Laplace's equation. This gives $\mu = -\sigma/r$ for $r \geq R$, and $\mu = -\sigma/R$ for $r \leq R$. Using equation (2.16) then gives

$$\frac{dR}{dt} = \nu = -\frac{1}{2}\left[\frac{\partial\mu}{\partial r}\right]_{R-\epsilon}^{R+\epsilon} = -\frac{\sigma}{2R^2}, \tag{2.17}$$

and thus Model B scales differently than Model A,

$$L(t) \sim t^{1/3} \tag{2.18}$$

This law has also been experimentally verified.[21] A recent experiment is due to Malik *et al.*.[31] They studied the coarsening of phase domains in a sodium borosilicate glass undergoing phase separation, using scattering with coherent x-rays. To analyze the fluctuations in the exact structure factor, they used a two-time correlation function defined by

$$C(q,t_1,t_2) = \frac{< I(t_1)I(t_2) > - < I(t_1) >< I(t_2) >}{[< I^2(t_1) > - < I(t_1) >^2]^{1/2}[< I^2(t_2) > - < I(t_2) >^2]^{1/2}} \tag{2.19}$$

Here $I(t)$ is the intensity in the pixel corresponding to the wave vector $\vec{q}$ at time t normalized to the total intensity. Simulations of domain coarsening using a Langevin model have found that τ, the correlation time (the time required for the scaled intensity covariance to decay to half its maximum value), follows this scaling law

$$\tau(q,t_1,t_2) = [t_{max}(q) - t_0]W_2(x), \tag{2.20}$$

where t_{max}, t_0, and $x = \delta t/\bar{t}$ ($\delta t = |t_2 - t_1|$ and $\bar{t} = (t_2 + t_1)/2$) are determined by the scaling behavior of the average structure factor $< I >$.

In the limit of large x, the scaling function W_2 is found to have a power-law form $W_2 = ax^p$ where $p = 1 - n$ and n was found to be worth $1/3$. Theoretically, the two-time intensity covariance is found to depend on δt only through $\delta t/\bar{t}$ in the small-$\bar{t}$ limit and $\delta t/\bar{t}^{1-n}$ in the large-$\bar{t}$ limit, based on simulations of Model B.[10]

2.5 Free-energy and Model Used in the Present Simulation

Many studies of convective flow of fluids, copolymers or other topics, mention the appearance of hexagonal or striped patterns on their samples.[25][43] To model the physical characteristics of these various experiments, we have chosen to use a free-energy described by equation (2.3) and model A. More precisely, our free-energy can be written as:

$$F[\phi] = \int d^d x \{ -\frac{1}{2}\epsilon\phi^2 + \frac{1}{2}[q_0^2\phi + |\vec{\nabla}^2\phi|]^2 + \frac{1}{4}\phi^4 - B\phi \}, \tag{2.21}$$

where ϕ is a phase field that describes the crystal lattice, q_0 is a measure of the initial lattice spacing, ϵ is related to temperature, and B is equivalent to the magnetic field in Model A.[18]

Three lattice structures can be described by this free-energy:
hexagonal phase: $\phi = a[cos(qx)cos(\frac{qy}{\sqrt{3}}) + \frac{1}{2}cos(\frac{2qy}{\sqrt{3}})] + b$
striped phase: $\phi = asin(qx) + b$
constant phase: $\phi = a$,
where x and y are the spatial coordinates and a and b are constants determined by minimizing the free-energy. A measure of a variable lattice spacing, q, can also be determined by minimizing the free-energy. For the hexagonal phase, F is found to be o minimum for three different values of q: 0, $\frac{\sqrt{3}q_0}{2}$, and $\frac{-\sqrt{3}q_0}{2}$. The former value is uninteresting and the latter unphysical, leaving $q = \frac{\sqrt{3}q_0}{2}$. For the striped phase, the free-energy is minimized for $q = 1$. Throughout this entire work, q_0 is chosen to be unity.

We consider a non-conserved order parameter, a variant of Model A, and hence time evolution obeys (see equation (2.4))

$$\frac{\partial\phi}{\partial t} = \epsilon\phi - ({q_0}^4\phi + 2{q_0}^2|\vec{\nabla}^2\phi| + |\vec{\nabla}^4\phi|) - \phi^3 + B. \tag{2.22}$$

Note that if we perform a transformation of the type $\phi \rightarrow \psi + C$, C being a constant, we can eliminate the constant B in the previous expression, but introduce a term in ϕ^2. Boyer and Viñals have used this equivalent expression to simulate hexagonal patterns.[7] Both equations (2.21) and (2.22) have $(\phi, B) <-> (-\phi, -B)$ symmetry.

Below we illustrate the minimum free-energy as a function of B for a specific value of $\epsilon = 0.8$, and the regions of stability for the stripe, hexagonal and constant phases, as a function of ϵ and B. The minimum free-energy, in the first graph is obtained by minimizing the expression of the free-energy as a function of a and b for the hexagonal and stripe phases and as a function of a for the constant phase. The values for ϵ and B used in all the simulations of this thesis were respectively $\frac{4}{15}$ and -0.2.

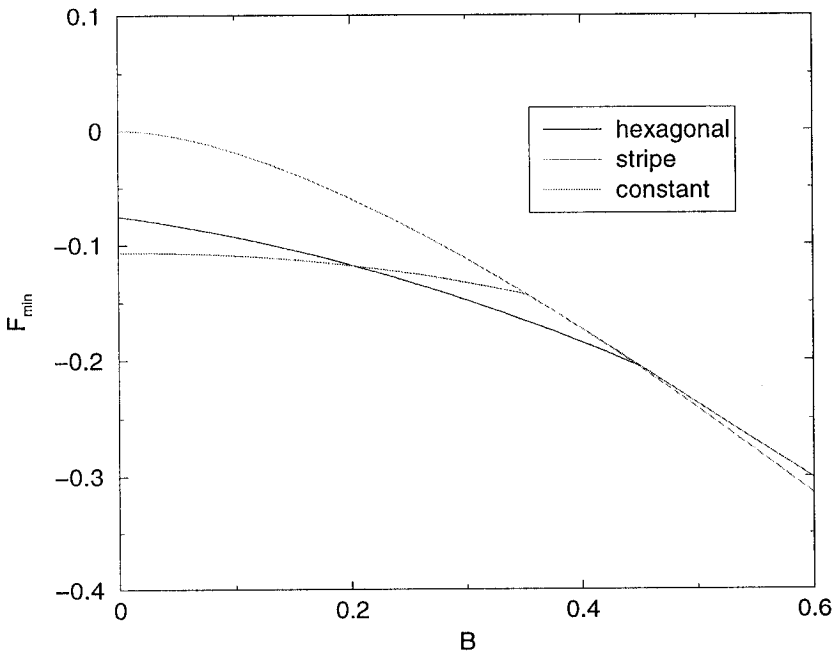

Figure 2.3: Minimum free-energy as a function of B ($\epsilon = 0.8$).

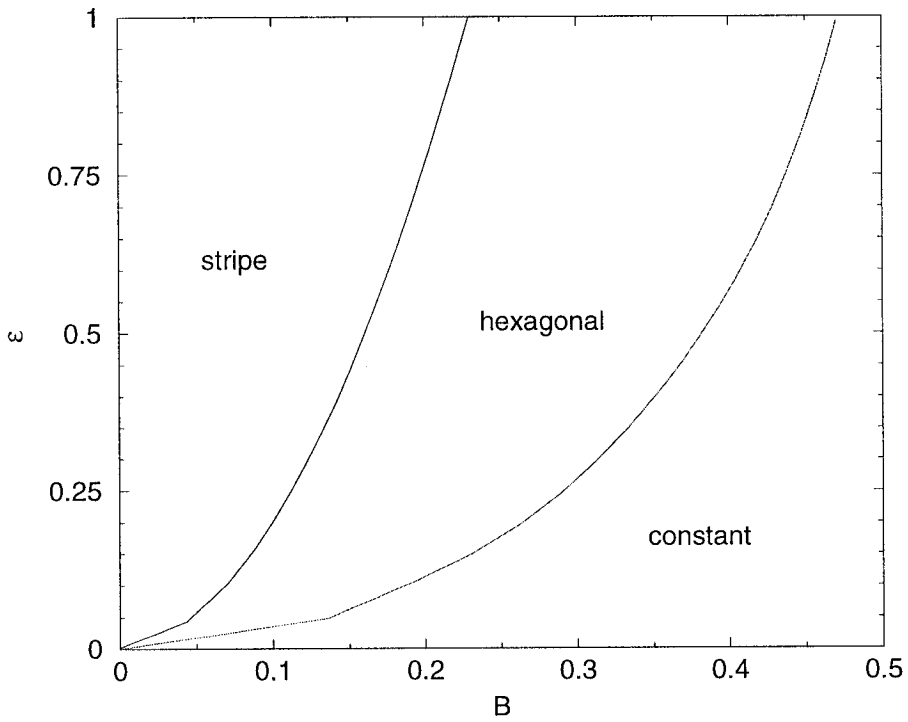

Figure 2.4: Regions of stability for the stripe, hexagonal and constant phases, as a function of ϵ and B. The point $(\epsilon, B) = (4/15, 0.2)$ corresponds to a hexagonal phase ground state.

2.5.1 Elastic Energy

As mentioned in the introduction, the model defined above can describe a solid with a hexagonal atomistic lattice. The elastic energy for a solid is

$$F_{el} = \frac{1}{2} \int d^d x K_{ijkl} u_{ij} u_{kl} \tag{2.23}$$

where K_{ijkl} is a constant tensor which simplifies depending on symmetry. For an isotropic of hexagonal solid, we have:
$K_{ijkl} = K_{klij} = K_{jikl} = K_{ijlk} = K_{jilk}$ and $K_{ijkl} = \lambda \delta_{ij} \delta_{kl} + \mu(\delta_{ik}\delta_{jl} + \delta_{il}\delta_{jk})$, λ and μ being the Lamé coefficients. As for u_{ij}, it is the linearized strain tensor and is defined as $u_{ij} = \frac{1}{2}(\nabla_i u_j + \nabla_j u_i)$, the u_i's being the displacements from the equilibrium position.[14]

We can now introduce definitions for the elastic moduli of a solid. Elastic moduli are defined as $C_{ik}(q) = K_{ijkl}q_j q_l$, where we have used the fact that $u_{ij}(q) = (iq_i u_j + iq_j u_i)/2$. Elastic moduli were calculated for the present model to be[18]

$$C_{12} = C_{44} = C_{11}/3,$$

where $C_{12} = [(3\bar{\psi} + \sqrt{15\epsilon - 36\bar{\psi}^2})q_0^2]^2/75$, which are consistent with an isotropic solid. Let us recall that $C_{11} = C_{xxxx} = C_{yyyy}$, $C_{12} = C_{xxyy}$ and $C_{44} = C_{xyxy}$.[2] For these coefficients, the Poisson ratio is $\nu = 1/3$ and the shear modulus is $\mu = C_{44}$. The change in energy for bulk, shear, and dilational deformations for an isotropic solid are, respectively, $(C_{11} + C_{12})\xi^2$, $(C_{44}/2)\xi^2$, and $(C_{11} - C_{12})\xi^2$, where ξ is the relative displacement for the different deformations.

Chapter 3

Review of Experimental and Theoretical Studies of Similar Systems

Two-dimensional hexagonal patterns have historically been studied in fluid systems. In fact, since the experimental work of Bénard on thermal convection in fluids at the beginning of the century[4], spatial and temporal pattern formation in the field of hydrodynamic instabilities has attracted great experimental and theoretical interest. In particular, in Rayleigh-Bénard and Bénard-Marangoni experiments, we witness the appearance of rolls and hexagonal patterns.

The Rayleigh-Bénard problem deals with the confinement of a liquid between the rigid boundaries of a shallow horizontal pool, while it is heated from below. When slightly heated, the fluid remains at rest, but when a critical heating is reached, buoyancy forces create convective motions. In most cases, a pattern of rolls parallel to the shorter side of the vessel will be induced by these motions. We witness a slightly different behaviour of the fluid when the upper surface of the liquid pool is free. Indeed, surface-tension variations with temperature will also act as a destabilizing mechanism. Then, as shown theoretically by Nield[34], convective motions occur because of buoyancy and surface-tension forces, leading to the appearance of hexagonal patterns. This particular case is known as the Bénard-Marangoni instability.

Other hexagonal patterns have been witnessed in different experiments. For example, Turing patterns[35], which have a possible relationship to biological phenomena, can also exhibit hexagonal or striped patterns. These special patterns are defined as stationary patterns localized along a band in a gel reactor containing a concentration gradient in reagents. They are similar to hydrodynamic patterns but of particular interest because they possess an intrinsic wavelength.

Theoreticians are evidently very interested in finding ways of simulating these different situations, they were in fact originally more particularly interested by the wavelength selection problem. As a means to do so, the Swift-Hohenberg equation was introduced. It was originally developed to model the onset of a convective instability in simple fluids (Rayleigh-Bénard instability). The initial idea was to consider the set of equations for a simple fluid in the Boussinesq approximation (incompressible fluid with density $\rho = \rho_0[1 - \alpha\Delta T])$, bounded by two infinite horizontal plates separated by a distance d, at temperatures T and $T + \Delta T$, respectively. In dimensionless units, the Swift-Hohenberg equation is

$$\frac{\partial\phi(r,t)}{\partial t} = [\epsilon - (1 + \nabla^2)^2]\phi(r,t) - \phi^3(r,t) + \xi(r,t), \tag{3.1}$$

where ϕ is a scalar two-dimensional field related to the amplitude of the eigenfunction corresponding to the unstable mode and is commensurate with the convective rolls. The quantity ξ is a random field that follows a Gaussian distribution, with zero mean and correlations corresponding to $2k_BT\delta(\vec{x} - \vec{x'})\delta(t - t')$ and $\epsilon = (R - R_c)/R_c$ acts as a control parameter. R is the Rayleigh number defined as

$$R = \frac{\alpha g \Delta T d^3}{\kappa\nu}, \tag{3.2}$$

where α is the thermal expansion coefficient, g is the acceleration of gravity, ν the kinetic viscosity, κ the thermal diffusivity and d the plate separation or the depth of the vessel. R_c ($\simeq 1708$) is the critical Rayleigh number at which an instability leading to convective rolls occur.[17]

Note that even if we have not identified them as Swift-Hohenberg related, equations already introduced in the first section indeed exhibit a strong resemblance to this equation. Also, equation (3.1) does not form hexagons

but rather stripes. Only when non-Oberbeck-Boussinesq convection takes place (general properties of the fluid all depend on temperature), can we witness the appearance of hexagons, described by equation (2.22).

To introduce the topic of defects, let us mention that in hexagonal patterns, the most common defect is the penta-hepta defect (PHD), in which a pentagonal cell and a neighboring heptagonal cell are paired together and embedded in a lattice of otherwise hexagonal cells.[45] PHDs are bound states in which two of the three modes have dislocations with opposite winding numbers. The formation of PHDs will be discussed in greated detail later.[38]

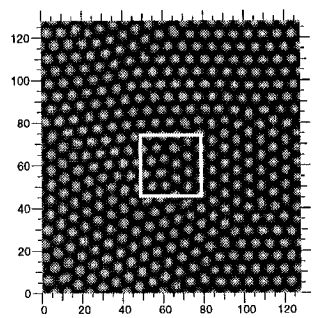

Figure 3.1: An example of a 128x128 surface we simulated, after 1000000 iterations

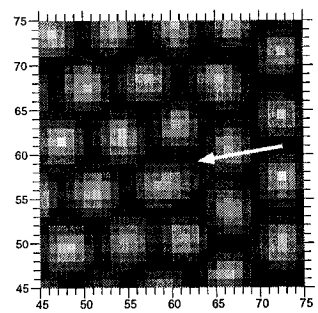

Figure 3.2: Small region of the previous graph showing a penta-hepta defect

3.1 Studies Related to the Bénard-Marangoni Convection and Penta-Hepta Defects Motion

An experimental study aimed at understanding the wavelength selection mechanism in Bénard-Marangoni convection was conducted by Cerisier *et al.* in 1987.[13] They mainly studied the influence of the vessel form, the aspect ratio (the ratio between the radius of the vessel and its height) and the heating gradient on the wavelength selection mechanism in an hexagonal pattern. They observed that λ, the wavelength, fluctuates randomly around a fixed value in all considered cases. They also noticed that for two different liquid depths, λ increases linearly with ϵ where $\epsilon = (R - R_c)/R_c$.

Four years later, Bodenschatz *et al.* published an experimental study, in a cylindrical cell of aspect ratio 86, of the transition between conduction, hexagons, and rolls in non-Boussinesq convection of gaseous CO_2.[6] Near onset ($\epsilon << 1$), they measured the size of the small hysteresis loop between conduction and hexagons. Above onset, they observed a perfect hexagonal pattern containing approximately 5000 convective cells. Hexagonal patterns in nonequilibrium extended systems are formed as a result of the superposition of three plane waves oriented at 120° with respect to each other and the flow can be described by three coupled amplitude equations where A_k, A_l and A_m describe slow variations of modulus and phase of periodic roll solutions with wave vectors q_k, q_l and q_m, where $\sum q_i = 0$ $(i = k, l, m)$ and $|q_i| = q_c$. Considering

$$\phi \propto \sum_{j=1}^{3} A_j exp(iq_j r) + c.c., \tag{3.3}$$

for a homogeneous pattern the simplest phenomenological amplitude equations read as

$$\dot{A}_k = \epsilon A_k - \alpha A_l A_m - \gamma(A_l^2 + A_M^2)A_k - A_k^3, \tag{3.4}$$

where the other two equations are obtained by circular permutation of k, l, m. $\epsilon = R/R_c - 1$ and expressions for α and γ are functions of the critical Rayleigh number, the Prandtl number and the

non-Oberbeck-Boussinesq parameter. (This equation was discussed in more detail by Rabinovich, whose study is presented later in this section.) Bodenschatz *et al.* found that the transition from perfect hexagons to rolls and vice versa was only very weakly hysteretic. It occurred when the two states had nearly the same value of generalized potential Φ defined as $\partial_t A_i = -\partial\Phi/\partial A_i$ derived from amplitude equations, instead of being triggered by instabilities.[11]

In 1993, Bestehorn published a paper[5] aimed at computing an evolution in space and time of patterns in Bénard-Marangoni convection. He furthermore explored the region of stability of hexagons and rolls with respect to spatially homogeneous amplitude instabilities and spatially nonuniform phase instabilities. We have already mentioned that in the case of Bénard-Marangoni convection, there are additional instabilities present compared to the case of convection between two rigid plates. In fact, the transition from rolls to hexagons, and vice versa as amplitude instabilities, are then seen. We also notice the appearance of sideband instabilities which restrict the variation of the size of stable hexagons drastically to a small band close to the critical wavelength. Using two particular solutions of the amplitude equations, namely rolls and hexagons, Bestehorn computed stability boundaries depending on the wavelength of these patterns and the distance from threshold (see figure 3.3).

Tsimring, in a Physical Review Letter published in 1995, focused on the role of defects in the problem of ordering and wavelength selection.[45] He argues that the motion of penta-hepta defects is caused by the ambient strain due to the deviation of the wave numbers from the onset value (thus providing a wave number selection mechanism), or by defect interaction. Tsimring investigated the motion of penta-hepta defects in slightly nonoptimal hexagonal patterns and their interaction. He used an amplitude equation formalism similar to equation (3.3) and (3.4), supplemented with gradient terms. According to Tsimring, spontaneously formed hexagonal patterns are usually defect ridden. Non-PHD defects are not stable and either transform into basic penta-hepta defects or simply vanish quickly. Furthermore, when two PHDs meet, they do not necessarily anihilate themselves, but may induce a different topologically structured PHD. A particular penta-hepta defect was studied using a 256x256 grid with periodic boundary conditions. It follows from these results that the

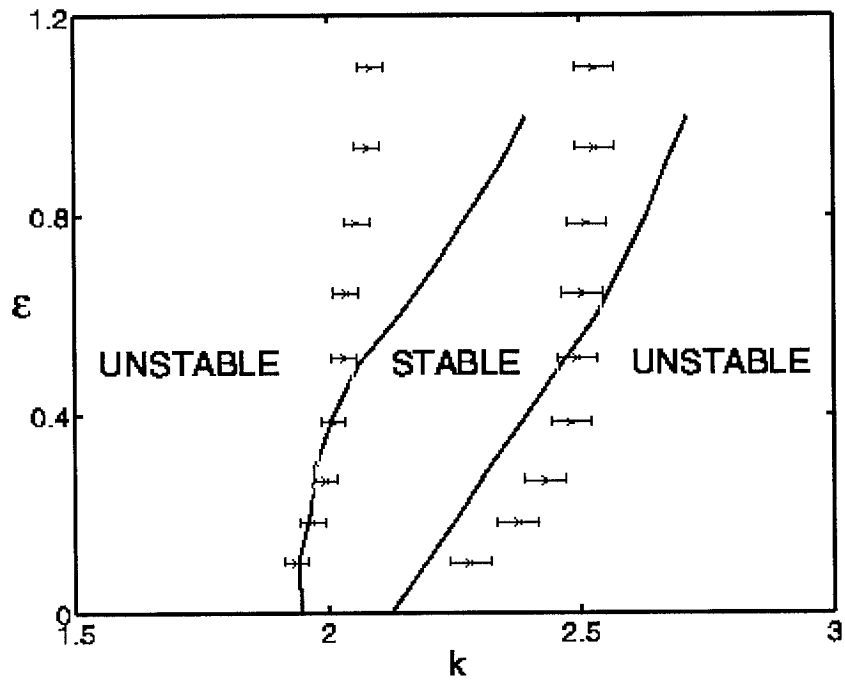

Figure 3.3: The band of stable wave numbers k for ideal hexagonal patterns ($k = k_1 = k_2 = k_3$) is shown for a range of reduced temperatures ϵ. The experimentally determined stable wave numbers lie between the low and high k boundaries and are compared with the theoretical predictions (solid lines) of Bestehorn[5].

movement of the PHDs depend on the relative misorientation angle θ, between perfect hexagonal patterns. It was also shown that the relative velocities V between two PHDs depends on their separation r as $V \sim r^{-1}$, which leads to $r \propto T^{1/2}$.

Very recently, Semwogerere and Schatz conducted a Bénard-Marangoni convection experiment on defect formation and motion in nonequilibrium hexagonal patterns.[43] Defects are presented in this paper as key elements in the process of pattern selection. Thermal laser writing, a new optical technique, was used to imprint the initial desired pattern and both the wave number selection and, most importantly, the defect propagation in the sample were subsequently studied. In fact, to determine the band of stable

pattern wave numbers, they imprinted an initial pattern of ideal hexagons. As well, initial patterns containing an isolated penta-hepta defect were imposed to study the directions and velocities of the defect propagation. Semwogerere and Schatz have found that the defect typically moves in a way that selects a wave number close to the center of the stable band. In particular, the direction of the propagation movement is strongly related to the wave numbers. Outside the band (see figure 3.3), ideal hexagons are unstable. PHDs and other less common point defects, consequently, typically form either at the lateral boundary, or in the bulk, and propagate rapidly throughout the pattern inducing disorder. This experiment has also showed that the defect motion is time dependent, but they mention their results cannot be explained by Tsimring's model.

Tam *et al.* have also studied the structure and propagation properties of a penta-hepta defect in an hexagonal pattern.[44] The latter was formed by inducing the formation of a layer of soap bubbles on a flat glass plate. They found that it is the defect's own structure which determines its direction of propagation.

Ciliberto *et al.* published a letter in 1990 concerned with the defects of a system where hexagons and rolls are both stable solutions.[16] They used three coupled Ginzburg-Landau equations (see equations (3.3) and (3.4)) to explain the competition between hexagons and rolls. These equations determine the behavior of the three complex amplitudes A_i of the sets of rolls describing the hexagonal structure. The dynamical system thus possesses four kinds of stationary solutions: the conductive state ($\phi = O$), rolls, hexagons, and the mixed state. They further showed that the unstable solution appears in the core of the defects of convective patterns, where the competition between the hexagonal and the roll symmetries takes place. Let us futhermore note that the penta-hepta defect can be seen locally as a roll. Following the same idea, hexagons will arise locally from a grain boundary between two oblique rolls. It is therefore clear that these defects play the role of nucleation seeds for the other phase, and thus are important in describing the dynamics of the transition between these two symmetries. These results were also confirmed in a convective experiment.

In 1994, Rabinovich and Tsimring published an article which studied numerically the propagation behavior and interaction of dislocations of roll

systems forming hexagonal patterns.[38] To describe the simultaneous growth of three rolls oriented at 120^o to each other, they used a set of three resonantly coupled Newell-Whitehead-Segel equations (the same as eq. (3.4))

$$\partial_t A_i = \epsilon A_i + \alpha A_j^* A_k^* - (|A_i|^2 + \gamma |A_j|^2 + \gamma |A_k|^2) A_i.$$

Here, $\{i, j, k\} = \{1, 2, 3\}, \{2, 3, 1\}, \{3, 1, 2\}$, ϵ is a small supercriticality parameter, $\alpha = 0(\epsilon^{1/2})$ is the coefficient of quadratic nonlinearity describing non-Boussinesq effects, and $\gamma = 0(1)$ is the ratio of the coefficient of cubic interaction of rolls of different orientation to the coefficient of cubic self-interaction. For $\alpha = 1.0$, the parameters favoring hexagons over rolls, the amplitudes of all three roll sets grow, and their phases get synchronized to form an hexagonal structure. However, the presence of the dislocation affects the synchronization process in an uncommon manner. If we start with two dislocations belonging to two different roll structures, the dislocations seem to move toward each other along a curved corridor and they eventually merge to form a penta-hepta defect. It was also found that the propagation trajectories of the dislocations and the position of the penta-hepta pair depend strongly on the initial phase distribution.

3.2 Other Related Experimental Studies

Ouyang and Swinney published a letter in Nature on the formation of Turing patterns. The patterns appeared spontaneously in a thin disc-shaped gel in contact with a reservoir of reagents of the chlorite-iodide-malonic acid reaction.[35] The pattern was detected optically through transparent glass. Initially, there are many transient yelow circles growing in a blue background. Within an hour, the propagation of the patterns slowly stopped leaving a clear field for the appearance of a yellow dot pattern evolving more slowly. A nearly stationary state thus emerged, with domains of hexagonal patterns separated by grain boundaries which moved very slowly. When using different acid concentrations, stripes rather than hexagons were observed for different acid concentrations. They furthermore determined the wavelengths of the hexagonal and striped patterns by performing spatial fast Fourier transforms. They noticed the wavelengths varied continuously with changes in the control parameters. As mentioned earlier, the wavelength is an intrinsic property of the reaction-diffusion system, not a consequence of the finite size of the system. It thus distinguishes Turing patterns from other well known nonequilibrium structures such as convection rolls or Taylor vortices.

In 2001, Purvis and Dennin reported an experimental measurement of the growth of regular domains evolving from an irregular pattern in electroconvolution.[37] They performed two types of measurements: they measured the full width at half maximum of the structure factor, and the domain wall length. They asserted the late-time growth of the domains was consistent with the power law t^n with n dependent on the method of measurement. The measurements using the structure factor were consistent with $t^{1/5}$, whereas those using the domain wall length were consistent with $t^{1/4}$ growth. The discrepancy between those results could come from the fact that the peak of the structure factor is itself not constant in time. Thus the 1/5 exponent may only be a transient. Indeed, we shall see a similar behavior in our data presented in the following chapter.

Another interesting study was conducted by Christopher Harrison *et al.*, aimed at understanding the ordering dynamics of the striped patterns of a single layer of cylindrical block copolymer microdomains in a thin film.[25] For a given local orientation of the stripes, $\theta(r)$, we can define the following

orientational correlation function

$$g_2(r) =< e^{2i\theta(r)}e^{-2i\theta(0)} >= e^{-r/\xi_2(t)}, \tag{3.5}$$

from which we can extract the orientational correlation length (ξ_2) of the pattern. The latter was measured as a function of annealing time of dislocations to quantitatively characterize the degree of microdomain order, suggesting a fractional kinetic exponent of 1/4. To motivate this exponent, they explain that if the distance between two dislocations is r, $E \sim 1/r$ (the strain energy) and the force $F \sim 1/r^2$. Consequently, for dissipative motion, $v \sim F \sim 1/r^2$ or in other words, $dt \sim r/v \sim r^3$ and thus, $t_f - t_i \sim r^4$ and $L \sim (t_f - t_i)^{1/4}$.

3.3 Other Related Theoretical studies

Bahiana and Oono published a paper twelve years ago presenting a different theoretical approach to ours, but applied to solve a similar problem.[3] In their study of striped patterns in block co-polymers, they decided to use the following modified Cahn-Hilliard equation

$$\frac{\partial \phi}{\partial t} = \Delta(-\tau\phi + u\phi^3 - D\Delta\phi) - B\phi, \tag{3.6}$$

to illustrate the movement of equal size polymer subchains covalently grafted together but with a weak repulsion between the subchains. D represents the lamellar thickness, τ and u are positive phenomenological parameters, τ being a measure of the quench depth, and B is a constant. Above T_c ($\tau < 0$), a and b subchains mix to make a uniform disordered phase, but below T_c, and for $B \neq 0$, the subchains tend to segregate and form a stripe pattern. Due to the covalent bonds between the subchains, segregation is only possible locally to form a lamellar structure. The order parameter ϕ used in this calculation is defined as the local concentration difference of monomers a and b. The use of different values for the parameters a and b, the different monomer units, and the parameter D, the lamellar thickness, gives rise to different configurations, including hexagonal and striped patterns. The focus of their results is the time evolution of D and its scaling. After minimizing the free-energy, the lamellar thickness is found to be proportional to $B^{-\frac{1}{3}}$ for sufficiently large D, and the domain size scales like $t^{1/3}$, consistent with Model B scaling. Bahiana and Oono also point out the need for a better modeling technique, even though theirs had a more thorough physical motivation in comparison to previous mesoscale models.

In 1991, further studies of pattern selection in Swift-Hohenberg equations was undertaken by Jorge Viñals *et al.*[46] They used the following equation describing the temporal evolution of a dynamic variable $\phi(x,t)$ as a function of a space variable x and time t,

$$\frac{\partial \phi(x,t)}{\partial t} = \left[\gamma^2 - (1 + \frac{\partial^2}{\partial x^2})^2\right] \phi(x,t) - \phi^3(x,t) + \xi(r,t), \tag{3.7}$$

where $0 \ll x \ll L$ and $\xi(x,t)$ is a Gaussian stochastic process. Both the deterministic and stochastic Swift-Hohenberg equation in one spatial

dimension were solved, and both using periodic boundary conditions. The one-dimensional equation can only model the appearance of straight and parallel convective rolls. For the deterministic case, $\Delta x = \frac{2\pi}{32}$ and $\Delta t = 10^{-4}$ chosen for stability considerations. The initial condition was chosen of approximate amplitude $|\phi(x,0)| \sim 10^{-2}$. Two regimes could be identified, an initial linear regime and a nonlinear regime evolving towards a configuration characterized by a unique wavelength. The study of the stochastic Swift-Hohenberg equation is motivated in part, by the issue of pattern selection in the presence of random fluctuations. The latter are important during the early stages after the instability, for a range of time that depends on the relative amplitude of the fluctuations and on the solution itself. At intermediate times, the structure factor stays broad and its maximum value varies with time, reflecting the nonlinear competition among the configuration $\phi_i(t)$ and the various Fourier components. At late times, the asymptotic stationary structure factor remains wide, indicating that the stationary configurations cannot be characterized by a single wave number. The two-dimensional Swift-hohenberg equation was later studied by Elder *et al.* for which they found a scaling law proportional to $t^{1/4}$.[19]

Very recently, Denis Boyer and Jorge Viñals published a letter concerning grain boundary motion in patterns with crystalline symmetry.[7] They focussed their study on a coarse grained model of a hexagonal pattern, and, in particular, on the motion of a grain boundary separating two domains with arbitrary misorientation. They used the following Swift-Hohenberg model of Rayleigh-Bénard convection with an additional quadratic term to allow the formation of hexagonal patterns

$$\frac{\partial \phi}{\partial t} = \epsilon\phi - \frac{1}{k_0^4}(k_0^2 + \nabla^2)^2\phi + g_2\phi^2 - \phi^3. \tag{3.8}$$

Again, adding a constant to ϕ leads to equation (2.22), as studied in this thesis. The order parameter $\phi(\vec{x},t)$ is related to the vertical velocity at the midplane of the convective cell, ϵ is the reduced Rayleigh number, and g_2 can be related to deviations from Boussinesq behavior in the working fluid. For $\epsilon > 0$, the uniform solution $\phi = 0$ becomes unstable and we witness the appearance of a periodic pattern characterized by a layer spacing $\lambda_0 = 2\pi/k_0$. Hexagonal patterns are stable for $-|\epsilon_m(g_2)| < \epsilon < \epsilon_m(g_2)$ whereas roll patterns need $\epsilon > \epsilon_m$. Boyer and Viñals found that defect motion is generically opposed by a pinning force, that is induced by

nonadiabatic corrections to the standard amplitude equations. It is mainly the misorientation angle between adjacent domains which determines the magnitude of this force: the most easily pinned grain boundaries are those with a low angle (typically $4^0 \leq \theta \leq 8^0$). They also found

$$D\dot{x}_{gb} = -p_{hex} sin[2k_0 x_{gb} sin(\theta/2)], \tag{3.9}$$

where $x_{gb}(t)$ is the time-dependent position of the grain boundary, D is a friction coefficient and p_{hex} is the amplitude of a pinning force.

Also in 2002, Ken Elder *et al.* have introduced a model very similar to the one we are using but for a conserved order parameter. The free energy and equation of motion look like

$$F = \int d\vec{r}\{\phi[(q_0^2 + \nabla^2)^2 - \epsilon]\phi/2 + \phi^4/4\}, \tag{3.10}$$

and

$$\partial\phi/\partial t = \nabla^2(\delta F/\delta\phi) + \eta, \tag{3.11}$$

where η is a stochastic noise with zero mean and correlations corresponding to $2k_B T\nabla^2\delta(\vec{x} - \vec{x'})\delta(t - t')$, and the field ϕ represents the local mass.[18] This model uses the analogy between localized hexagons and atoms in an hexagonal lattice to simulate elastic and plastic behavior of crystals on atomic length scales while considerably increasing speeds of calculation. For example, the current model can simulate one diffusion time in 1000 time steps, while it would require $\sim 10^9$ time steps for molecular dynamics simulations. Elder *et al.* verified numerically Read and Shockley's predictions[39] concerning the energy per unit surface length, E_L, between grains whose orientations differ by an angle θ. Indeed, they also found that $E_L = E_M\theta[1 - ln(\theta/\theta_M)]$, where E_M and θ_M are constants. They also showed that nucleation of dislocations in epitaxial growth is highly correlated with surface buckling. Thus, it must be considered when calculating the critical thickness to obtain a quantitatively correct expression. Also, the surface roughness decreases after dislocations appear. The relationship between this model and the elastic energy theory has been done in section (2.5.1).

In 1997, an article entitled "Interfaces of Modulated Phases" was published by Netz, Andelman and Schick, whose purpose was to numerically study tilt

grain boundaries within lamellar phases and interfaces between coexisting modulated phases of different symmetry: lamellar (L), hexagonal (H) and disordered (D) phases.[33] The dimensionless free-energy they used was

$$F[\phi] = \int \left\{ -\frac{\chi}{2}\phi^2 + \frac{1-\phi}{2} ln \frac{1-\phi}{2} + \frac{1+\phi}{2} ln \frac{1+\phi}{2} - \frac{1}{2}(\nabla\phi)^2 + \frac{1}{2}(\nabla^2\phi)^2 - \mu\phi \right\} dV. \quad (3.12)$$

The enthalpic term, proportional to the interaction parameter χ, favors an ordered state in which $|\phi| \neq 0$. The equation also includes an entropy of mixing preferring a disordered state, $\phi = 0$, and confining $|\phi|$ to be less than unity, and derivatives of the order parameter. The modulation of a dominant wave vector $q^* = 1/\sqrt{2}$ will also induce the ordered state because of the competition between the negative gradient square term and the positive Laplacian square. We only need to perform an expansion around $\phi = 0$ to relate this free-energy to the one used in this thesis. Let us now give results only related to the hexagonal-disordered and hexagonal-lamellar interface. The corresponding interfacial energy $\gamma_{HD} \sim (\chi - \chi_C)^{\mu_*}$ (where $\chi_C = 3/4$ corresponds to the triple point of coexistence of all phases) of the former scales with $\mu_* = 2$, and the corrugation of the lamellae near the interface of the latter resembles that seen in experiments on diblock copolymers blends. γ_{HL}, the interfacial free energy of this interface, scales with the classical critical exponent $\mu_* = 3/2$. This illustrates that the hexagonal and lamellar phases are locked into a fixed relative position with respect to translations normal to the H-L interface (different from the case of L-D and H-D interfaces).

Chapter 4

Simulation Description and Results

The challenge of understanding phase-ordering dynamics is to find the nature of the late-time solutions of differential equations such as equation (2.22), subject to random initial conditions. Let us recall equation (2.22) goes as

$$\frac{\partial \phi}{\partial t} = \epsilon\phi - ({q_0}^4\phi + 2{q_0}^2|\vec{\nabla}^2\phi| + |\vec{\nabla}^4\phi|) - \phi^3 + B.$$

Indeed, the precise form of the initial conditions should not be important as long as only short-range spatial correlations are present. Thus the initial conditions of the surfaces used in the different simulations were a set of random values between -1.0 and 1.0. These values, one for each lattice point, were generated using ran1, a well-known random number generator.[36]

The grid used in the present simulation was squared shaped with periodical boundary conditions. Dimensions of either 128x128, 256x256 or 512x512 lattice points were used for different types of studies. The spatial and temporal steps were $dx = dy = 1.0$ and $dt = 0.04$ and the incrementation was done using a simple Forward Euler scheme. The values for $dx = dy$ and dt follow this law

$$\Delta t < \frac{(\Delta x)^4}{16 - 2(\Delta x)^2} \tag{4.1}$$

to assure stability.[41] As already mentioned, concerning the following simulations, $q_0 = 1$, $\epsilon = 4/15$ and $B = -0.2$.

The C language was the programming language used throughout the entire process of data collecting and analyzing. Also, the program dfourn, easily available in Numerical Recipes in C[36], was used, with a few modifications, to compute the Fourier Transforms and Inverse Fourier Transforms. Using Message-Passing Interface commands, the program was also parallelized into four different squared shaped sub-grids to increase effectiveness. Finally, the finite difference equations used to compute equation (2.4), the laplacian and the biharmonic in the simulations were the following:

$$dt\_phi[i][j] = dt*(\epsilon*\phi_{[i][j]} - (q_0^4*\phi_{[i][j]} + 2*q_0^2*lap_{[i][j]} + bihar_{[i][j]}) - \phi_{[i][j]}^3 + B), \tag{4.2}$$

$$lap[i][j] = \frac{\phi_{[i+1][j]} + \phi_{[i-1][j]} - 2*\phi_{[i][j]}}{dx^2} + \frac{\phi_{[i][j+1]} + \phi_{[i][j-1]} - 2*\phi_{[i][j]}}{dy^2}, \tag{4.3}$$

and

$$bihar[i][j] = \frac{\phi_{[i+2][j]} + \phi_{[i-2][j]} - 4*(\phi_{[i+1][j]} + \phi_{[i-1][j]}) + 6*\phi_{[i][j]}}{dx^4} + \frac{\phi_{[i][j+2]} + \phi_{[i][j-2]}}{dy^4} +$$

$$\frac{-4*(\phi_{[i][j+1]} + \phi_{[i][j-1]}) + 6*\phi_{[i][j]}}{dy^4} + \frac{2*(\phi_{[i+1][j+1]} + \phi_{[i+1][j-1]} + \phi_{[i-1][j+1]} + \phi_{[i-1][j-1]})}{(dx*dy)^2} +$$

$$\frac{-4*(\phi_{[i+1][j]} + \phi_{[i-1][j]}) - 4*(\phi_{[i][j+1]} + \phi_{[i][j-1]}) + 8*\phi_{[i][j]}}{(dx*dy)^2}. \tag{4.4}$$

This chapter will now deal with simulation results and analysis. First, studies concerning the structure factor will be presented. This is followed by an analysis of results concerning surface energies. Last but not least, a study of temporal correlations will close the chapter.

4.1 Structure Factor Results and Analysis

Let us first take a look at an example of the evolution of a surface with time, starting with a randomly distributed surface. From left to right and from top to bottom, the surfaces respectively represent instants after 50, 200, 400, 750, 1000, 5000, 10000, 100000, 1000000 iterations. We first notice the appearance of bumps on the surface, followed by an organization of the latter into hexagonal patterns.

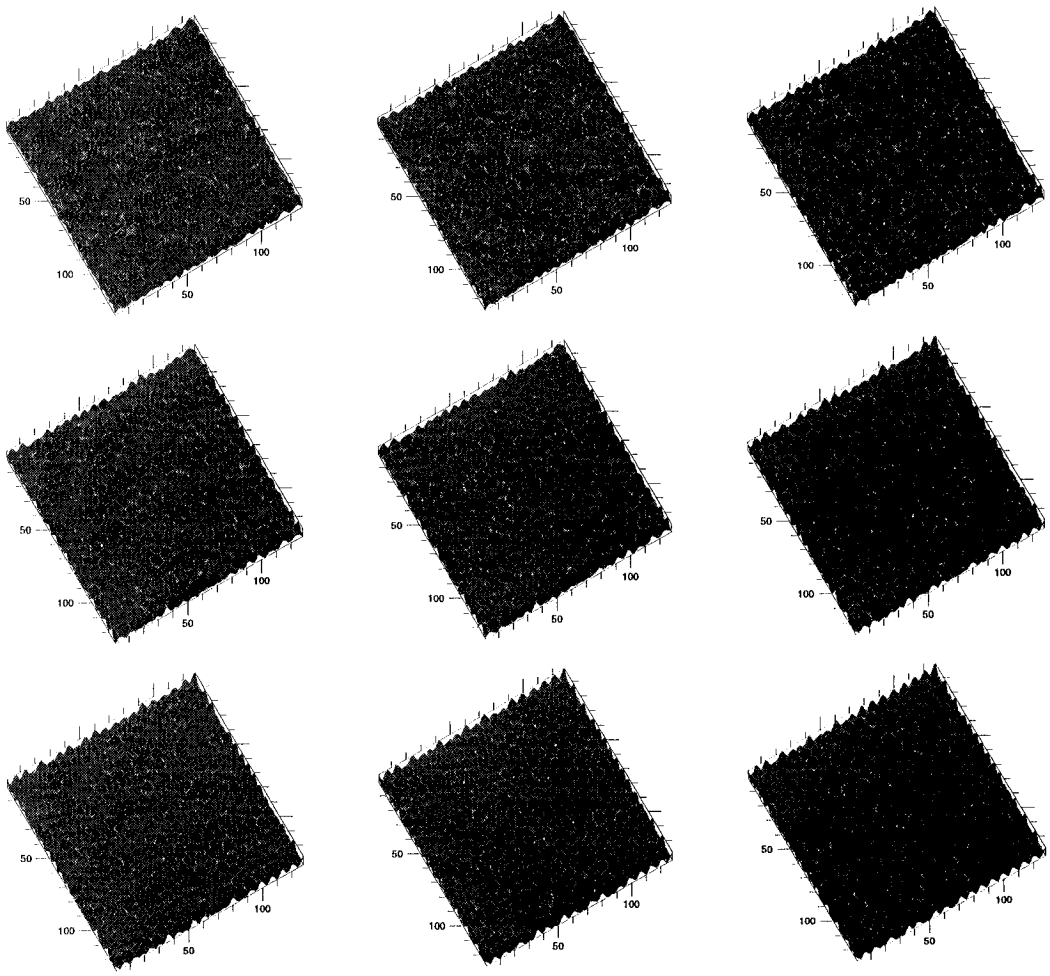

Figure 4.1: Example of the evolution of a surface with time

One can further use these surfaces to compute structure factors $S(\vec{k},t) =< \phi_{\vec{k}}(t)\phi_{-\vec{k}}(t) >$. In Fourier space, structure factors can be represented by rings in unorganized systems or by a pattern of hexagonal dots for perfectly hexagonally patterned surfaces. The following figures respectively represent structure factors of surfaces after 200 and 500000 iterations and of a surface covered by a nearly perfect hexagonal pattern.

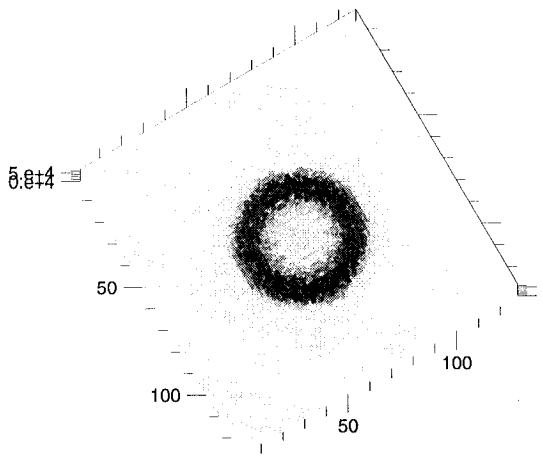

Figure 4.2: Fourier transform of a surface after 200 iterations

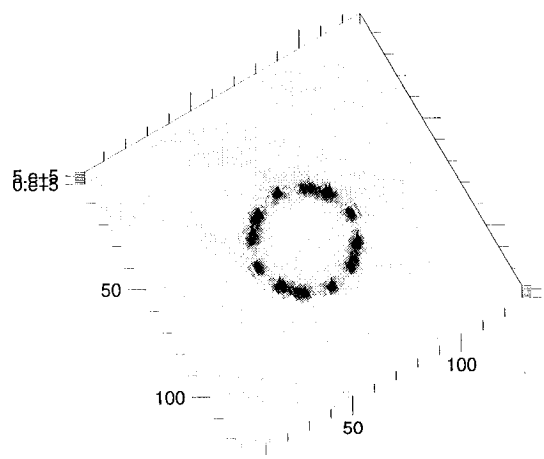

Figure 4.3: Fourier transform of a surface after 500000 iterations

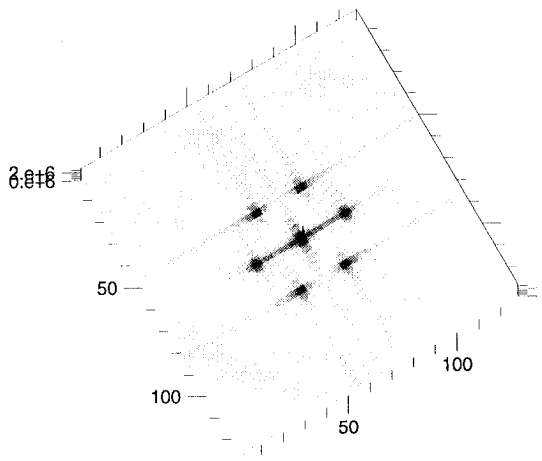

Figure 4.4: Fourier transform of a surface covered by a nearly perfect hexagonal pattern

To consider the structure factor of the surfaces at various instants, we take a radial cut of the ring in Fourier space, i.e. starting at the center and moving outward, we consider k_z as a function of only k_x for example. We thus end up with a peak representing the structure factor at $k = k_x$. We then move around the ring and add 360 of those slices together, one per degree, and then divide by 360 to give a circular average. The result is evidently a peak, the structure factor circularly averaged. This peak can easily be fitted with the following formula to standardize the results: a Lorentzian plus a Lorentzian squared,

$$f = \frac{a(2)}{(x - a(3))^2 + a(1)^2} + (\frac{a(2)}{(x - a(3))^2 + a(1)^2})^2. \tag{4.5}$$

The parameters a(1), a(2) and a(3) can be varied and fitted independently (see fig. (4.5)).

This fitted peak will have a smaller maximum amplitude and a larger full width at half maximum for unorganized systems, the amplitude increasing and the full width half max decreasing with the appearance of hexagonal patterns. The two following figures represent this circular average of the structure factor for two distinct times, after 200 iterations and after 500000 iterations.

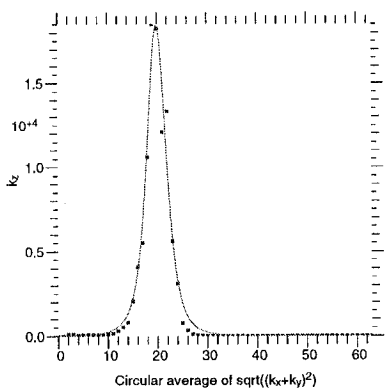

Figure 4.5: Structure factor circularly averaged over the entire ring in Fourier space, after 200 iterations, fitted with equation (4.5)

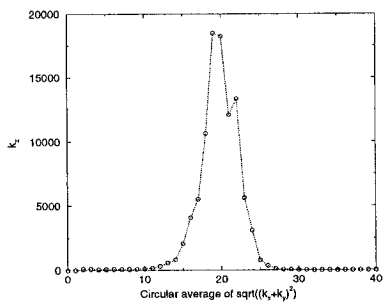

Figure 4.6: Structure factor circularly averaged over the entire ring in Fourier space, after 200 iterations. Line to guide the eye.

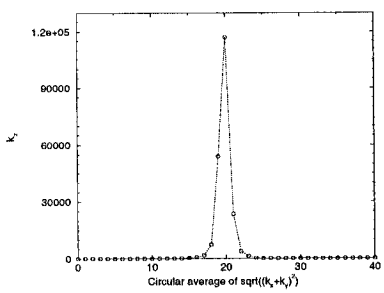

Figure 4.7: Structure factor circularly averaged over the entire ring in Fourier space, after 500000 iterations. Line to guide the eye.

Now, consider a graph of the evolution of the structure factor's maximum amplitude with time. Each curve in the following graph is an average of ten idependent runs, all having evolved from an initially different randomly distributed surface. Also, each curve represents the evolution of the structure factor's amplitude with time, for a particular grid dimension, either a 128x128, a 256x256 or a 512x512 lattice point grid. We can thus compare how differently the evolution of the amplitude of the structure factor occurs for different grid dimensions. The following expression was used to compute the amplitude as a function of $a(1)$, $a(2)$ and $a(3)$:

$$A = (a(2)/(a(1)^2)) + ((a(2)^2)/(a(1)^4)).$$

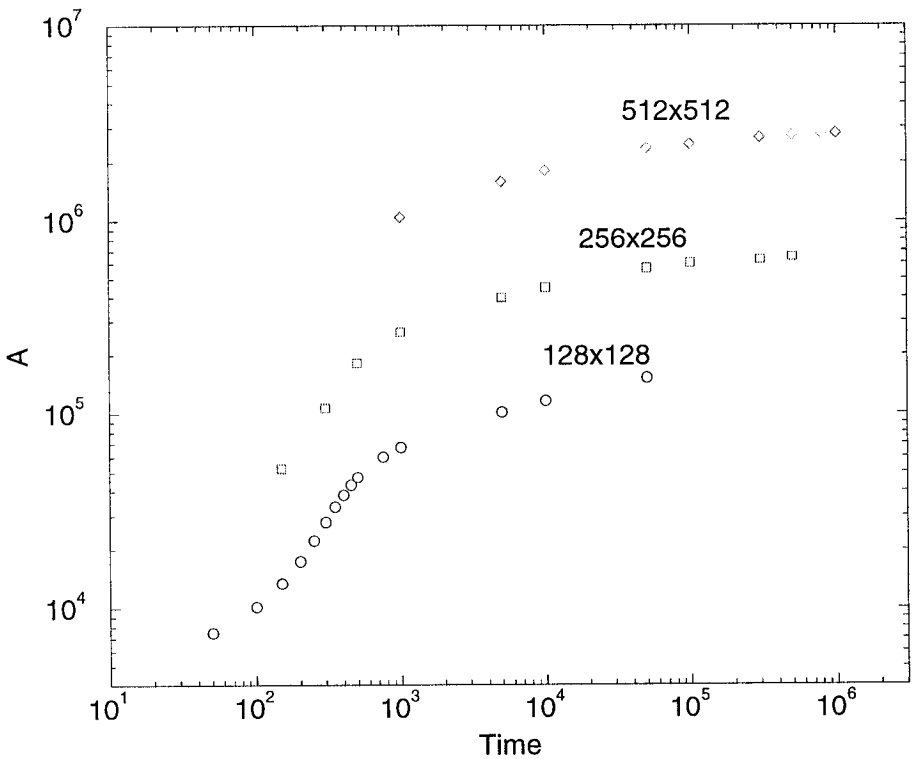

Figure 4.8: Maximum amplitude of the structure factor as a function of time for three different grid dimensions. Each curve is an average of ten independent runs.

The same exercise was done for the full width at half maximum of the structure factor. Each curve is again an average of 10 independent runs, all having evolved from an initially different randomly distributed surface. Also, each curve represents the data for a particular grid dimension, either a 128x128, a 256x256 or a 512x512 lattice points grid. Logarithmic scales were again used for both the x and the y axes to permit an easier comparison between the three curves. The following expression was used to compute the full width at half maximum as a function of $a(1)$, $a(2)$ and $a(3)$

$$\delta_k = \frac{a(1)*\sqrt{\pm(a(1)^2+a(2))*(-a(2)+\sqrt{2*a(2)^2+a(1)^4+2*a(2)*a(1)^2})}}{a(1)^2+a(2)}$$

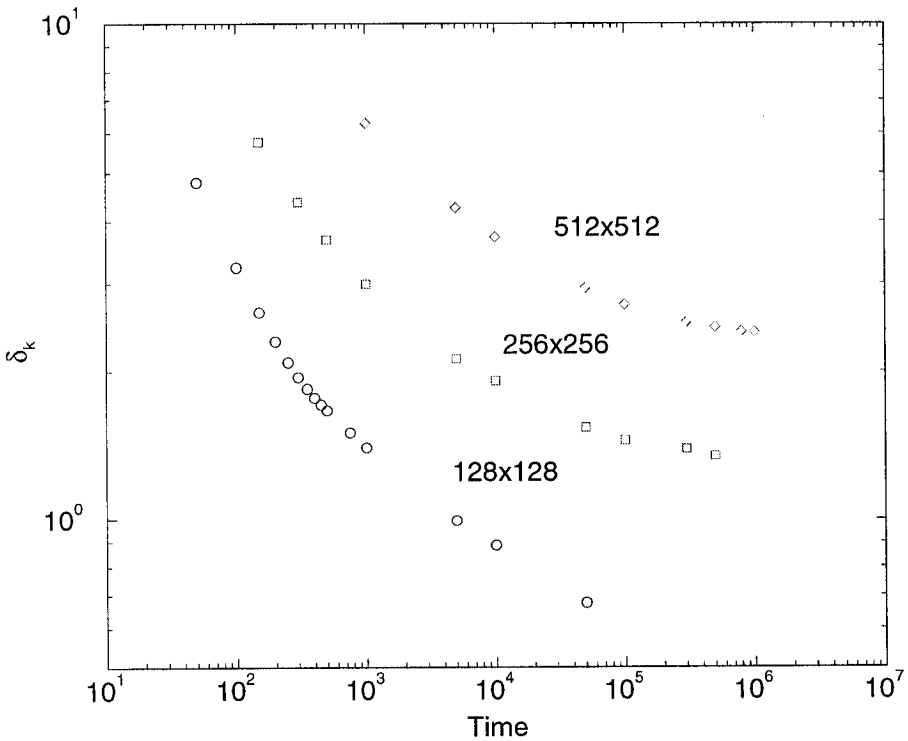

Figure 4.9: Full width at half maximum of the structure factor as a function of time for three different grid dimensions. Each curve is an average of ten independent runs.

We can furthermore investigate possible scaling laws for the maximum amplitude, and the full width at half maximum of the structure factor. The scaling laws could be deduced from trials at superposing the different curves on the two previous graphs. We indeed transformed graph (4.8) into (4.10) and graph (4.9) into (4.11) to deduce the two following laws

$$A(t, L) = L^2 f(t), \tag{4.6}$$

and

$$\delta_k(t, L) = L f(\frac{t}{L^{1/2}}). \tag{4.7}$$

Concerning the former equation, we can clearly see it is scaling as the dimension of the space: the number of domains increases as L^2. Also, we notice the presence of two regimes: early time and a late time, the latter either following a power law or a $\ln t$ form.

Concerning δ_k, early time behaviour can be described by the expression $t^{-1/3}$, whereas late time follows more closely $t^{-1/10}$. Two lines with those respective slopes have been added to the graph to guide the eye. A third graph (fig. 4.12) has been added to show how closely the late time can be approximated by a logarithmic form. Indeed, it is interesting to note that both late time behaviours for the maximum amplitude and the full width at half maximum could be described by logarithmic forms. This indicates that the system becomes trapped in metastable configurations.

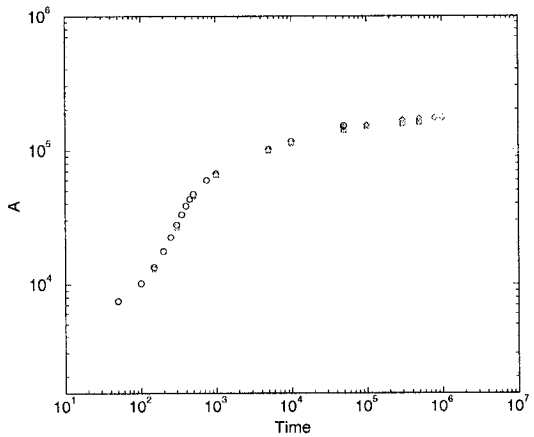

Figure 4.10: Scaled maximum amplitude of the structure factor as a function of time for the three different curves represented on graph (4.8)

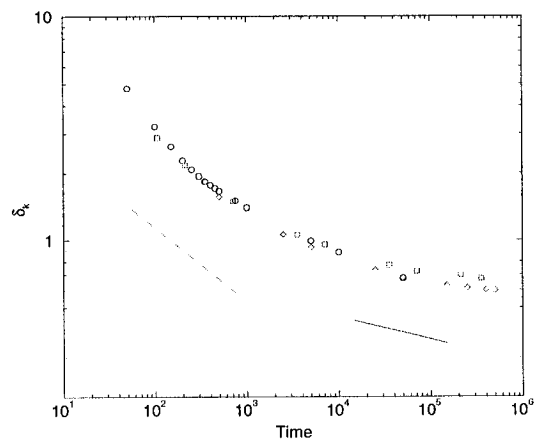

Figure 4.11: Scaled full width half max of the structure factor as a function of time for the three different curves represented on graph (4.9)

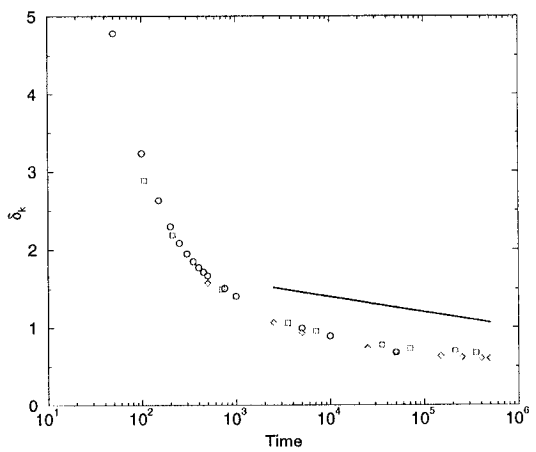

Figure 4.12: Scaled full width half max of the structure factor as a function of time for the three different curves represented on graph (4.9)

4.2 Surface Energy Results and Analysis

In this section, we give our results of a study concerning surface energy measurements. We wish to start by introducing the theory related to the energy of topological defects.[14] The latter energy can be divided into two separate categories: the core energy E_c and the elastic or the strain energy E_{el}. The core energy is associated with the destruction of the order parameter at the core of the defect. It is difficult to define, but we can identify its order of magnitude by considering the condensation energy f_{cond} of the ordered state. Indeed, the latter represents the increase in free energy per unit volume due to destruction of the order parameter. E_c is of order of the volume (or area) of the defect times f_{cond}. Thus, the core energy of a vortex in two dimensions is

$$E_c = Aa^2 f_{cond}, \tag{4.8}$$

where A is a numerical constant and a, the core radius. This is also the core energy per unit length of a vortex line in three dimensions.

The elastic energy is that associated with the slow variation of the elastic variable far from the core. It is defined as

$$E_{el} = \pi k^2 \rho_s ln(R/a), \tag{4.9}$$

where k is the winding number and R is the linear dimension of the sample. The total energy of the vortex is then

$$E_v = E_{el} + E_c. \tag{4.10}$$

We can use both the equation for the core energy and the equation for the elastic energy, minimizing with respect to a to find

$$\frac{-\pi k^2 \rho_s}{a} + 2aAf_{cond} = 0,$$

$$a^2 = \frac{\pi k^2}{2} \frac{\rho_s}{Af_{cond}} \sim k^2 \xi^2.$$

Thus, as expected, the core radius a is proportional to the correlation length ξ. The latter is defined as the distance over which ϕ changes.

The following equation, the discretized form of the local energy given by equation (2.21), was used to compute the energy at each lattice point of the surface

$$E[i][j] = -\epsilon * \frac{\phi^2_{[i][j]}}{2} + 0.5 * (\phi_{[i][j]} + lap_{[i][j]})^2 + 0.25 * \phi^4_{[i][j]} - B * \phi_{[i][j]}. \quad (4.11)$$

To calculate the energy of the entire surface, we used the following equation

$$E_{surface} = \frac{\sum_{i,j} E_{[i][j]} * (dx * dy)}{L^2} \quad (4.12)$$

where L is the size of the system. $E_{surface}$ is the global energy of the system per unit area.

We can first take a look at the representation of the energy of a surface for a 256x256 lattice point system, after 150, 1000 and 500000 iterations.

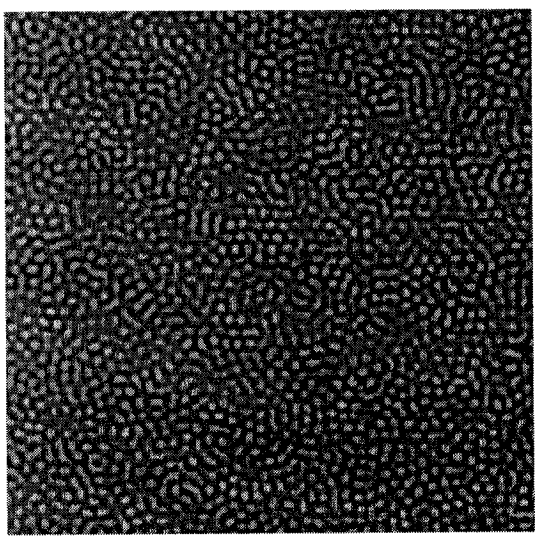

Figure 4.13: Representation of the energy of a 256x256 lattice point surface, after 150 iterations

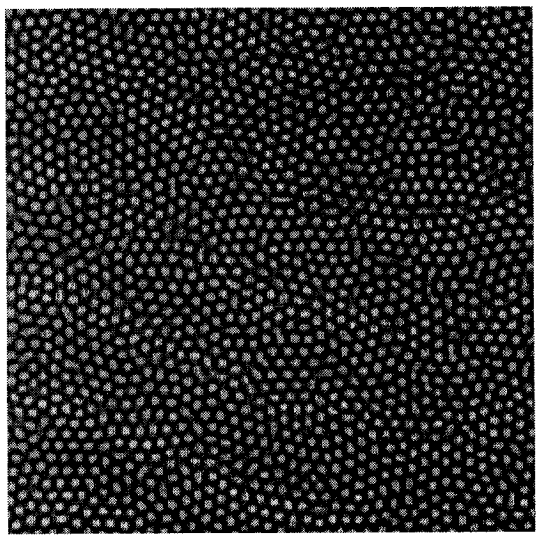

Figure 4.14: Representation of the energy of a 256x256 lattice point surface, after 1000 iterations

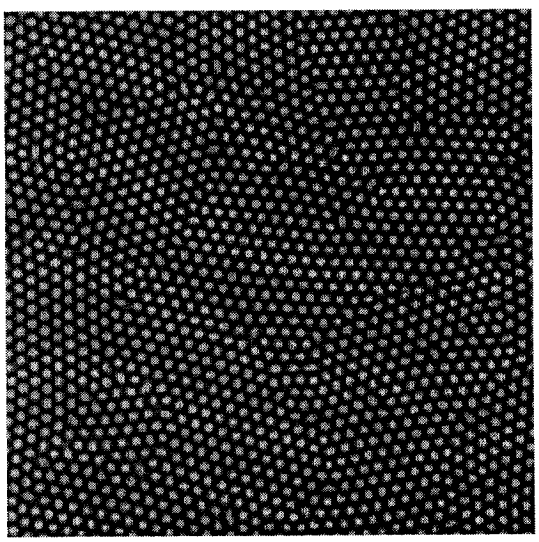

Figure 4.15: Representation of the energy of a 256x256 lattice point surface, after 500000 iterations

Now we can consider the surface energy (for each curve, divided by the area of the surface) as a function of time for different grid dimensions, 128x128, 256x256 and 512x512. Each curve on the following graph is an average of ten independent runs, all having evolved from an initially different randomly distributed. The black curve corresponds to the 128x128 system, the red curve to the 256X256 system and the green curve to the 512X512 system. Evidently, the actual energy values on the y axis are arbitrary.

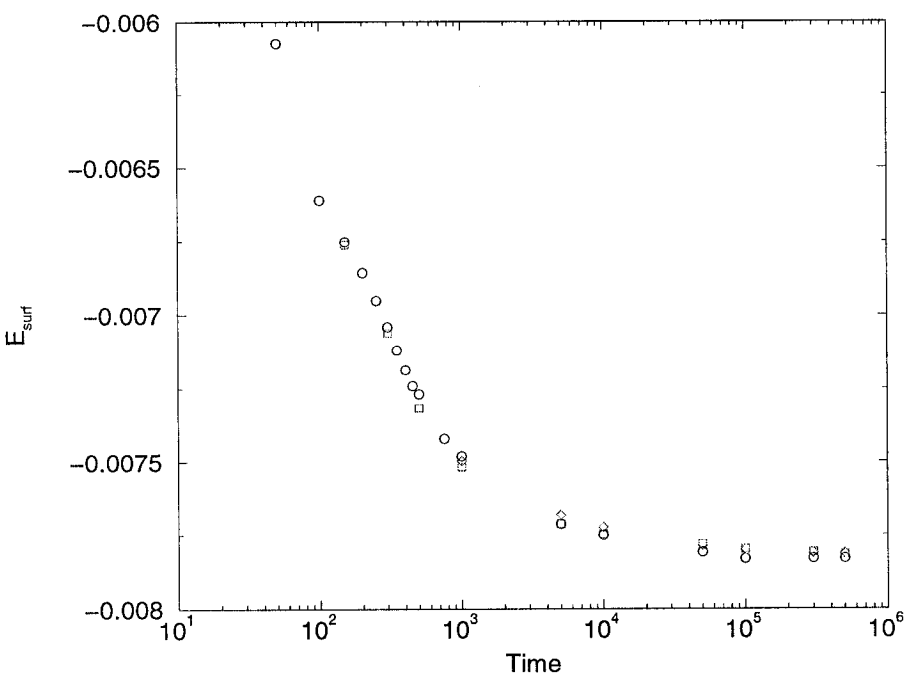

Figure 4.16: Surface energy as a function of time for three different grid dimensions. Each curve is an average of ten independent runs.

After having added a certain energy $E_\infty = 0.00784$ to all three curves in order to have only positive energies, we can look at the previous graph using a log-log scale. We can clearly see that the curves scale according to

$$E - E_\infty = At^{-1/2} \tag{4.13}$$

where A is a constant. A line of slope 1/2 has been added to the graph to guide the eye. The 1/2 exponent comes from the fact that we have a system where the order parameter is not conserved.

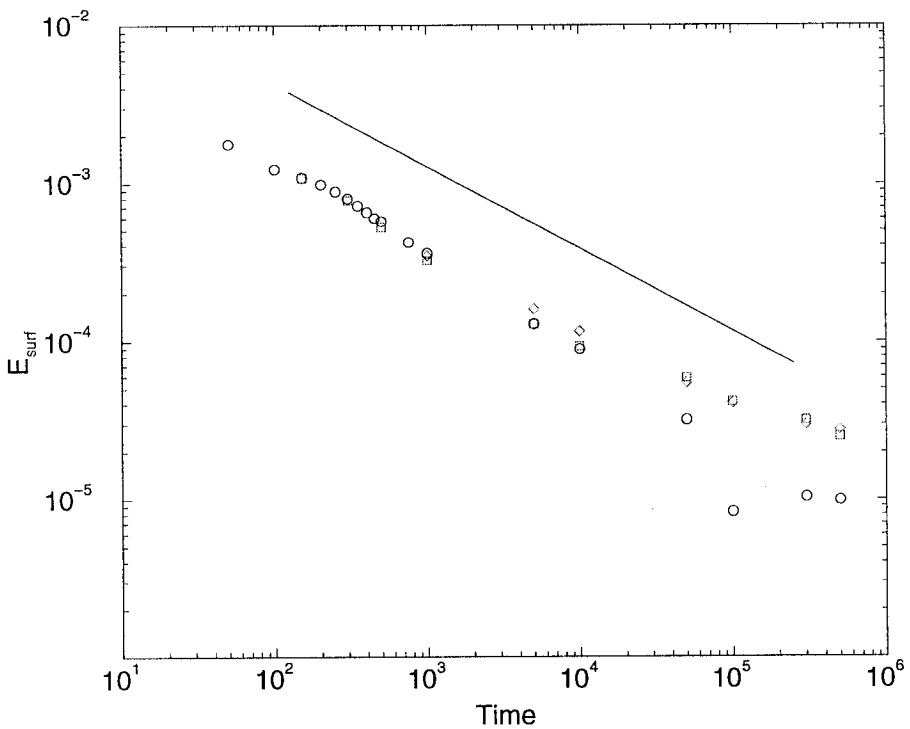

Figure 4.17: Scaled surface energy as a function of time for three different grid dimensions. Each curve is an average of ten independent runs.

4.3 Temporal Correlations Results and Analysis

In the present section, we consider at temporal correlations to extract information on the structure and movement of dislocations. To do so, we use a method already described in [27], that is, we consider two order parameter surfaces, 500 iterations apart, starting with surfaces after 5000 and 5500 iterations (fig. (4.18)). We then "substract" the two surfaces one from the other fig. (4.19) and perform a Fourier transform on this substraction. We then add the real part squared and the imaginary part squared of this Fourier transform and perform an inverse Fourier transform to end up with fig. (4.20), the correlation function in two-dimensions. If we now take a look at a slice of this previous graph, starting at the central peak and moving outward, we can compute a circular average of this slice, taking one slice every degree, moving around the circular peak. We end up with a circular average of the sideview of the correlation function, $C(r,t)$, fig. (4.21).

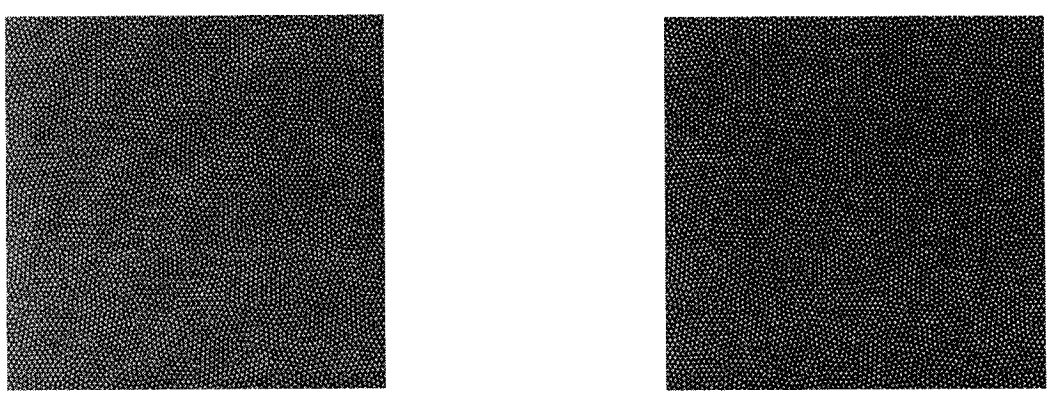

Figure 4.18: Example of surfaces after 5000 and 5500 iterations for a 512x512 size grid

Figure 4.19: Difference between two images of surfaces, taken respectively after 5000 and 5500 iterations

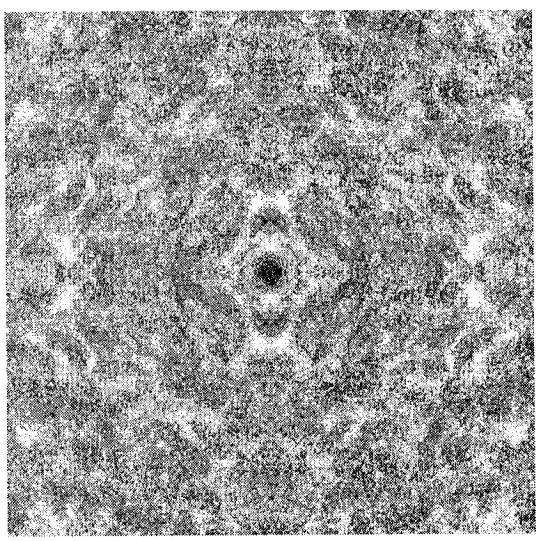

Figure 4.20: Fourier transform of the difference between two images of surfaces, taken respectively after 5000 and 5500 iterations

Usually, one would use the orientational correlation function to study the growth of domains caused by the motion of dislocations. As mentioned earlier, the orientational correlation function can be defined as

$$g_n(r) =< e^{ni\theta(r)}e^{-ni\theta(0)a} >= e^{-r/\xi_n(t)}, \tag{4.14}$$

for a given local orientation of the stripes, $\theta(r)$ ($n = 2$ for stripes, $n = 6$ for hexagons).[25][37] On the other hand, this method is very complicated and has not been proven to give better results than the study of temporal correlation functions. We have thus decided to use the latter to track dislocations and their correlation in space and time. This method also had the advantage of focussing solely on dislocations.

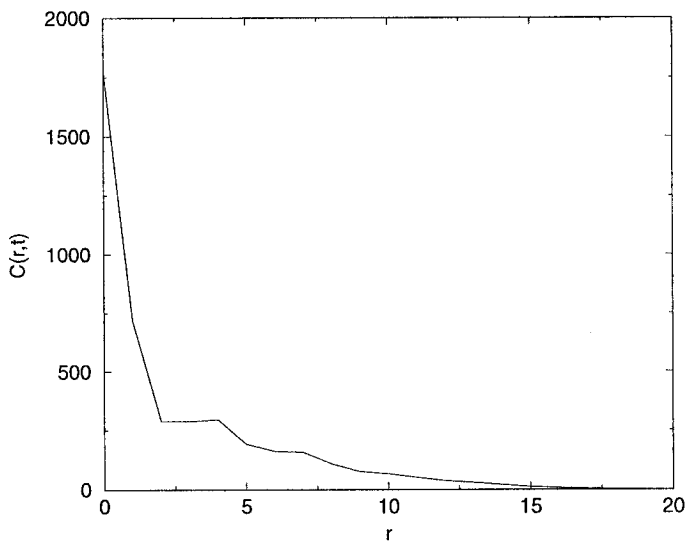

Figure 4.21: Circular average of the correlation function between two surfaces, taken respectively after 5000 and 5500 iterations

The following graph, fig. 4.22, is a linear-log graph of a collection of those circular averages of correlation functions. Each curve represents the correlation function of a different set of surfaces, i.e. the first curve represents the correlation function of surfaces after 5000 and 5500 iterations, the second curve, of surfaces after 5500 and 6000 iterations, and so on until the last curve, which is the correlation function of surfaces after 19500 and 20000 iterations. Also, each curve is an average of seventeen runs. We can give the following equations to help clarify the explanation

$$\tilde{S}_k(t) =< \phi_k(t_0+t)\phi_{-k}(t_0+t) > - < \phi_k(t_0)\phi_{-k}(t_0) >, \tag{4.15}$$

$$C(r,t) = \int dk e^{-2\pi i k t}\tilde{S}_k. \tag{4.16}$$

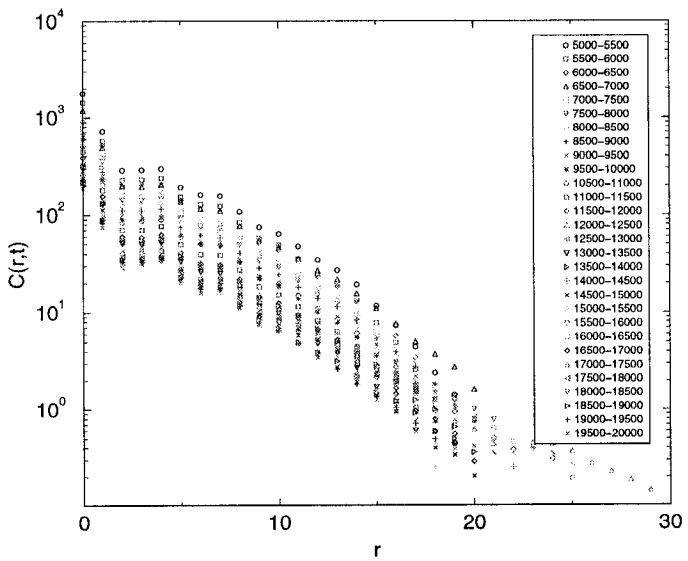

Figure 4.22: Collection of circular averages of correlation functions between two surfaces, each taken 500 iterations apart

We can now take a look at the scaled temporal correlation functions. The latter are represented on the following graph where we can easily see the three first curves, the correlation functions between surfaces after 5000 and 5500, 5500 and 6000, and 6000 and 6500, do not scale as well as the 26 other curves. We can thus separate the formation of the hexagons into two regimes. For earlier times ($t \leq 6000$), there is only a local reorganization of the field ϕ which is not necessarily related to the movement of dislocations, defaults and grain boundaries.

The later regime scales according to the following equation

$$C(r,t) \sim t^{\alpha} e^{-\beta r}, \tag{4.17}$$

where $\alpha = 1.0$ and $\beta = 0.25$. We have also added a line of equation $y = 5000 \exp(-0.25r)$ to the graph to guide the eye.

We can start by mentioning we cannot collapse completely the early time data. Indeed, the three or four curves which don't fall on the others, correspond to the earliest times considered (5500-5000 iterations, 6000-5500 iterations and 6500-6000 iterations). If we look at the full width at half maximum of the structure graph, we see that late time behaviour really starts around 6000 or 7000 iterations. Another explanation could be the finite interfacial width of the grain boundaries. The exponential behaviour of the scaling law means we have well defined structures, clearly shown on fig. (4.18), as opposed to fractal structures which would have power law correlations. As for the value of 1.0 found for α, we could explain it by imagining the structures moving around according to a random walk. We know that, in this case, the correlation function in real space is directly proportional to time.

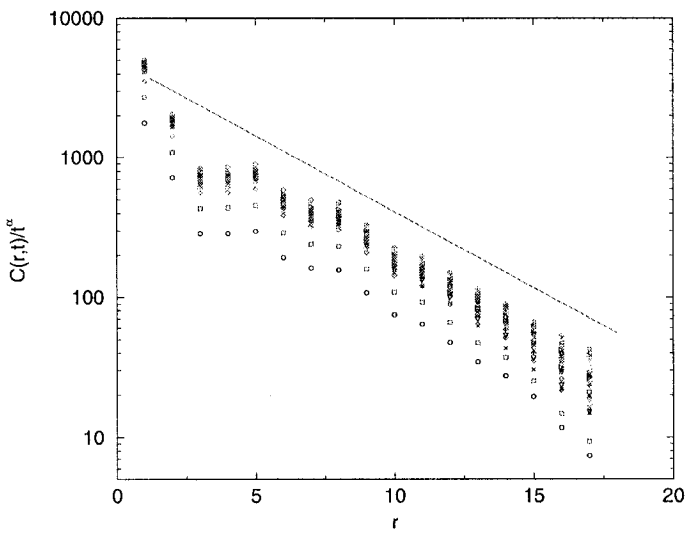

Figure 4.23: Scaled collection of circular averages of correlation functions between two surfaces, each taken 500 iterations apart. A line described by the equation $y = 5000 \exp(-0.25x)$ was added to lead the eye.

Chapter 5

Conclusion

To conclude this work, let us review the main results we have obtained. We have found there is a scaling law for the structure factor as a function of L, the system size, but there is no clear power law regime in time. As well, the amplitude depends on time in a complicated manner.

$$A(t, L) = L^2 f(t),$$

and

$$\delta_k(t, L) = L f(\frac{t}{L^{1/2}}).$$

For both the maximum amplitude and full width at half maximum scaling laws, there are two regimes present: early time and late time. And in both cases, late time behaviours could be described by logarithmic forms. This indicates that the system becomes trapped in metastable configurations.

As for the total energy of the system per unit area, it was found to be independent of the size of the system. It also follows a power law in time.

$$E - E_\infty = At^{-1/2}$$

The 1/2 exponent comes from the fact that we have a system where the order parameter is not conserved.

Concerning the last section, a technique performing a substraction between two surfaces taken at different times, was used to further study the

temporal correlation functions, focussing on the movement and structure of dislocations. The amplitude follows a power law in time but the spatial dependence is exponential.

$$C(r,t) = t^{1.0} e^{-0.25r}$$

The exponential behaviour of the scaling law means we have well defined structures. And concerning $\alpha = 1$, we explained it by suggesting the structures moving around according to a random walk.

With regards to further work, we note the following. This model is sufficient for fluid sustems (a Model A-like, non-conserved model) but to better simulate real solids, the use of a conserved order parameter should be considered. As well, further connection between the grain boundary motion and domain growth remains to be explored. Finally, it would be straightforward to extend this work to the study of three dimensional systems.

Bibliography

[1] S.M. Allen and J.W. Cahn. A Microscopic Theory for Antiphase Boundary Motion and Its Application to Antiphase Domain Coarsening. Acta Metallurgica, vol.27, p.1085 (1979).

[2] N.W. Ashcroft, N.D. Mermin. *Solid State Physics.* Saunders College, Philadelphia (1976).

[3] M. Bahiana and Y. Oono. Cell Dynamical System Approach to Block Copolymers. Physical Review A, vol.41, no.12, p.6763 (1990).

[4] H. Bénard. Rev. Gen. Sci. Pur. Appl., vol.11, p.1261 (1900).

[5] M. Bestehorn. Phase and Amplitude Instabilities for Bénard-Marangoni Convection in Fluid Layers with Large Aspect Ratio. Physical Review E, vol.48, p.3622 (1993).

[6] E. Bodenschatz, J.R. de Bruyn, G. Ahlers, and D. S. Cannell. Transitions between Patterns in Thermal Convection. Physical Review Letters, vol.67, no.22, p.3078 (1991).

[7] D. Boyer and J. Viñals. Weakly Nonlinear Theory of Grain Boundary Motion in Patterns with Crystalline Symmetry. (2002).

[8] A.J. Bray. Theory of Phase-Ordering Kinetics. Advances in Physics, vol.43, no.3, p.357 (1994).

[9] G. Brown, P.A. Rikvold, M. Sutton, and M. Grant. Speckle from phase-ordering systems. Physical Review E, vol.56, no.6, p.6601 (1997).

[10] G. Brown, P.A. Rikvold, M. Sutton, and M. Grant. Evolution of speckle during spinodal decomposition. Physical Review E, vol.60, no.5, p.5151 (1999),

[11] F.H. Busse. Journal of Fluid Mechanics, vol.30, p.625 (1967).

[12] J.W. Cahn, J.E. Hillard. Journal of Chemical Physics, vol.28, p.258 (1958).

[13] P. Cerisier, C. Pérez-García, C. Jamond, and J. Pantaloni. Wavelength Selection in Bénard-Marangoni Convection. Physical Review A, vol.35, no.4, p.1949 (1987).

[14] P.M. Chaikin and T.C. Lubensky. *Principles of Condensed Matter Physics.* Cambridge University Press, Cambridge (1995).

[15] S. Ciliberto, E. Pampaloni, and C. Pérez-García. Competition between Different Symmetries in Convective Patterns. Physical Review Letters, vol.61, no.10, p.1198 (1988). Errata: Physical Review Letters, vol.61, no.17, p. 2005 (1988).

[16] S. Ciliberto, P. Coullet, J. Lega, E. Pampaloni, and C. Pérez-García. Defects in Roll-Hexagon Competition. Physical Review Letters, vol.65, no.19, p.2370 (1990).

[17] M.C. Cross, P.C. Hohenberg. Pattern Formation Outside of Equilibrium. Journal of Materials Science Letters, vol.65, no.3, p.851 (1993).

[18] K.R. Elder, M. Katakowski, M. Haataja, and M. Grant. Modeling Elasticity in Crystal Growth. Physical Review Letters, vol.88, no.24, p.245701 (2002).

[19] K.R. Elder, J. Viñals, M. Grant. Dynamic Scaling and Quasiordered States in the Two-Dimensional Swift-Hohenberg Equation. Physical Review A, vol.46, no.12, p.7618 (1992).

[20] A. Fluerasu. Private communication.

[21] B.D. Gaulin, S. Spooner, Y. Morii. Phys. Rev. Lett., vol.59, p.668 (1987).

[22] N. Goldenfeld. *Lectures on Phase Transitions and the Renormalization Group.* Addison-Wesley Publishing Company, New York (1992).

[23] J.D. Gunton and M. Droz. *Introduction to the Theory of Metastable and Unstable States.* Springer-Verlag, New York (1983).

[24] J.D. Gunton, M. San Miguel, and P. Sahni. Dynamics of First-Order Transitions in *Phase Transitions and Critical Phenomena*, C. Domb and J.L. Lebowitz, vol.8, p.267. Academic Press, New York (1983).

[25] C. Harrison, D.H. Adamson, Z. Cheng, J.M. Sebastian, S. Sethuraman, D.A. Huse, R.A. Register, and P.M. Chaikin. Mechanisms of Ordering in Striped Patterns. Science, vol.290, no.5496, p.1558 (2000).

[26] P.C. Hohenberg and B.I. Halperin. Theory of Dynamic Critical Phenomena. Reviews of Modern Physics, vol.49, no.3, p.436 (1977).

[27] M. Karttunen, M. Haataja, K.R. Elder, and M. Grant. Defects, Order, and Hysteresis in Driven Charge-Density Waves. Physical Review Letters, vol.83, no.17, p.3518 (1999).

[28] K. Kawasaki. Diffusion Constants near the Critical Point for Time-Dependent Ising Models. I. Phys. Rev. vol.145, p.224 (1966).

[29] J.S. Langer. An Introduction to the Kinetics of First-Order Transitions in *Solids far from Equilibrium*, C. Godrèche, p.297. Cambridge University Press, Cambridge (1992).

[30] F. Livet, F. Bley, R. Caudron, E. Geissler, D. Abernathy, C. Detlefs, G. Grübel, M. Sutton. Kinetic Evolution of Unmixing in an AlLi Alloy using X-Ray Intensity Fluctuation Spectroscopy. Physical Review E, vol.63, p.36108 (2001).

[31] A. Malik, A.R. Sandy, L.B. Lurio, G.B. Stephenson, S.G.J. Mochrie, I. McNulty, and M. Sutton. Coherent X-Ray Study of Fluctuations during Domain Coarsening. Physical Review Letters, vol.81, no.26, p.5832 (1998).

[32] B. Morin, K.R. Elder, M. Sutton, and M. Grant. Model of the Kinetics of Polymorphous Crystallization. Physical Review Letters, vol.75, no.11, p.2156 (1995).

[33] R.R. Netz, D. Andelman, and M. Schick. Interfaces of Modulated Phases. Physical Review Letters, vol.79, no.6, p.1058 (1997).

[34] D.A. Nield. Journal of Fluid Mechanics, vol.19, p.1941 (1964).

[35] Q. Ouyang and H.L. Swinney. Transition from a Uniform State to Hexagonal and Striped Turing Patterns. Nature, vol.392, p.610 (1991).

[36] W.H. Press, S.A. Teukolsky, W.T. Vetterling, B.P. Flannery. *Numerical Recipes in C.* Cambridge University Press, New York (1999).

[37] L. Purvis and M. Dennin. Domain Coarsening in Electroconvection. Physical Review Letters, vol.86, no.26, p.5898 (2001).

[38] M.I. Rabinovich and L.S. Tsimring. Dynamics of Dislocations in Hexagonal Patterns. Physical Review E, vol.49, no.1, p.R35 (1994).

[39] W.T. Read and W. Shockley. Dislocation Models of Crystal Grain Boundaries. Physical Review, vol.78, p.275 (1950).

[40] S.R. Ren and I.W. Hamley. Cell Dynamics Simulations of Microphase Separation in Block Copolymers. Macromolecules, vol.34, no.1, p.116 (2001).

[41] T.M. Rogers. Domain Growth and Dynamical Scaling during the Late Stages of Phase Separation. Doctoral thesis of the University of Toronto, (1989)

[42] A.D. Rutenberg, B.P. Vollmayr-Lee. Anisotropic Coarsening: Grain Shapes and Nouniversal Persitence. Physical Review Letters, vol.83, no.19, p.3772 (1999).

[43] D. Semwogerere and M.F. Schatz. Evolution of Hexagonal Patterns from Controlled Initial Conditions in a Bénard-Marangoni Convection Experiment. Physical Review Letters, vol.88, no.5 (2002).

[44] T. Tam, D. Ohata, and M. Wu. Dynamics of a Penta-Hepta Defect in a Hexagonal Pattern. Physical Review E, vol.61, no.1, p.R9 (2000).

[45] L.S. Tsimring. Penta-Hepta Motion in Hexagonal Patterns. Physical Review Letters, vol.74, no.21, p.4201 (1995).

[46] J. Viñals, E. Hernández-García, M. San Miguel, and R. Toral. Numerical Study of the Dynamical Aspects of Pattern Selection in the Stochastic Swift-Hohenberg Equation in One Dimension. Physical Review A, vol.44, no.2, p.1123 (1991).